
Pre-main sequence accretion of low-mass stars in the Cesam2k20 code

Student
Ducheng Lu

Supervisors
Dr. Ludovic Petitedemange
Dr. João Pedro Cadilhe Marques
Dr. Louis Manchon
Dr. Charly Pinçon

June 2025

Contents

1	Introduction	1
2	Pre-main sequence magnetospheric accretion	2
2.1	Magnetospheric accretion paradigm	2
2.2	Observational evidence of magnetospheric accretion . . .	3
3	Stellar evolution modeling	4
3.1	Stellar structure equations	4
3.2	Pre-main sequence evolution	6
3.2.1	Pre-main sequence evolution with constant mass .	6
3.2.2	Pre-main sequence evolution with accretion	8
4	Methods	9
4.1	The consequences of accretion	9
4.1.1	Gravitational energy	10
4.1.2	Coordinate transformation for accretion modeling .	10
4.1.3	Deuterium from the accreted material	11
4.1.4	Hot and cold accretion	12
4.2	The stellar evolution code Cesam2k20	13
4.2.1	Lagrangian variables	13
4.2.2	Automatic location of grid points	14
4.2.3	Structure equations	15
4.2.4	PMS initial models	15
4.2.5	Input physics	16
4.3	Accretion in Cesam2k20	17
4.3.1	Homologous coordinates for Cesam2k20	17
4.3.2	Modifications to the structure equations	18
4.3.3	Adding deuterium to the accreted material	20
5	Results and discussions	20
5.1	Accreting vs. non-accreting stellar models	20
5.2	Dependence on the initial central temperature	23
5.3	Dependence on accretion rates	23
5.4	Dependence on deuterium abundance	25
5.5	The birthline	27
6	Conclusion	28
	References	31

Abstract

Context. Stars form from a small seed that grows by accreting material from its surrounding disk. Evolutions of pre-main sequence (PMS) stars are strongly influenced by accretion, which brings mass, energy, and chemicals to the star. Accretion processes are complex and not fully understood, necessitating a study of their impact on stellar evolution.

Aim. This project aims to investigate how accretion affects the structure and evolution of low-mass pre-main sequence stars by implementing accretion into the 1D stellar evolution code *Cesam2k20*.

Methods. I implemented accretion by modifying stellar structure equations to include mass, energy, and fresh deuterium from the accreted material. Stellar models were computed with varying final masses, initial central temperatures, accretion rates, and deuterium abundances, and the results were compared with non-accreting models and previous studies.

Results. Accreting protostars show evolutionary tracks distinct from non-accreting models, with early development strongly influenced by initial central temperature and deuterium abundance, while accretion rate has a minor effect. The study reproduces the protostellar birthline with some deviations linked to seed mass and input physics.

Conclusion. Implementing accretion highlights the importance of realistic modeling in understanding PMS evolution, laying groundwork for future improvements such as heat injection, variable accretion rates, and angular momentum.

Abstract

Contexte. Les étoiles se forment à partir d'une petite graine qui croît par accrétion de matière provenant du disque environnant. L'évolution des étoiles pré-séquence principale (PMS) est fortement influencée par l'accrétion, qui apporte masse, énergie et composés chimiques à l'étoile. Les processus d'accrétion sont complexes et mal compris, ce qui nécessite une étude de leur impact sur l'évolution stellaire.

Objectif. Ce projet vise à étudier comment l'accrétion affecte la structure et l'évolution des étoiles de faible masse de la séquence pré-principale en implémentant l'accrétion dans le code d'évolution stellaire 1D *Cesam2k20*.

Méthodes. J'ai implémenté l'accrétion en modifiant les équations de structure stellaire pour inclure la masse, l'énergie et le deutérium neuf provenant du matériau accréte. Des modèles stellaires ont été calculés avec des masses finales, des températures centrales initiales, des taux d'accrétion et des abondances en deutérium variables, puis les résultats ont été comparés à des modèles sans accrétion et à des études antérieures.

Résultats. Les protoétoiles accrétantes suivent des trajectoires évolutives distinctes, influencées principalement par la température centrale initiale et l'abondance en deutérium, le taux d'accrétion jouant un rôle plus modéré. La ligne de naissance protostellaire est reproduite, avec quelques écarts liés à la masse initiale et aux paramètres physiques.

Conclusion. La mise en œuvre de l'accrétion montre l'importance d'un modèle réaliste pour comprendre l'évolution PMS, posant les bases d'améliorations futures comme l'injection de chaleur, les taux variables et le moment cinétique.

1 Introduction

The formation of a low-mass star begins with the gravitational collapse of a cold dense region in a molecular cloud. When the self-gravity of such a region overcomes the opposing pressure and magnetic support, collapse begins (Larson 1969). This process is typically nonhomologous, with the central regions collapsing more rapidly than the outer ones.

Initially, the collapse is isothermal, as radiation efficiently maintains the thermal equilibrium of the system. As the density increases, the central region becomes increasingly opaque to radiation, inhibiting its escape from the core while still allowing it from the outer layers. This growing opacity leads to an adiabatic collapse of the center, during which the temperature and pressure rise until a first hydrostatic core is formed. Continued contraction raises the temperature until hydrogen molecules dissociate around 2000 K, triggering a second, rapid collapse. This ends with the formation of a denser, more compact hydrostatic object, or the protostar (e.g., Stahler and Palla 2004). The protostar then accretes material from the surrounding cloud, a process that can continue for several million years.

Once most of the surrounding material has been accreted, the protostar enters the pre-main sequence (PMS) phase and becomes visible as a T Tauri star (TTS). TTSs are cold PMS stars that serve as precursors to low-mass main-sequence stars of spectral types F, G, K, and M. Classical T Tauri stars (CTTSs) are characterized by strong infrared (IR) emission from their optically thick accretion disks. As accretion declines due to the depletion of material in the inner disk, the IR emission weakens, and the stars are then observed as weak T Tauri stars (WTTSs). Similarly, young massive stars are also expected to undergo accretion during their early evolution and are observed as Herbig Ae/Be stars—hotter and more luminous than TTSs. However, the accretion processes for these higher-mass stars remain poorly understood.

The earliest accretion stages remain observationally elusive, as protostars are deeply embedded in the surrounding dusty cloud, making it highly extincted in optical and near-IR wavelengths. Nonetheless, indirect indicators such as disks, outflows, and jets provide compelling evidence of ongoing accretion. Modeling these stages remains challenging due to the time-variable, non-linear nature of the process and the complexity of the underlying physics.

When Henyey et al. (1955) and Hayashi (1961) first studied the early phases of stellar evolution, accretion was not taken into account. Instead, stars were assumed to begin their evolution as fully convective objects with very large radii and luminosities, contracting under their own gravity until a radiative core developed, eventually reaching the main sequence. These evolutionary paths are now known as the Hayashi and Henyey tracks. Since Larson (1969) introduced the concept of the formation of a hydrostatic core, followed by continued accretion from an infalling envelope of gas and dust, accretion has been recognized as a fundamental process in early stellar evolution, supported by both theoretical and observational studies.

There has been growing interest in studying accretion in PMS stars since the discovery of exoplanetary systems, particularly because of its relevance to planetary formation. Accretion disks are the birthplaces of planets and other small bodies, making the study of accretion crucial for understanding the early evolution of planetary systems. Beyond this, accretion can significantly influence the internal structure and rotation of stars by supplying mass, energy, and chemicals. In particular, accretion sets the initial distribution of angular momentum, which influences the star's rotational evolution and internal dynamics. These structural and rotational changes can, in turn, affect the stellar dynamo

mechanism responsible for amplifying magnetic fields in young stars (e.g., Stelzer and Neuhauser 2001).

Accretion also impacts long-term stellar evolution by setting the initial conditions for subsequent evolutionary stages and can leave lasting imprints. Consequently, it can directly affect the determination of fundamental stellar parameters such as age, mass, and radius, which are crucial not only for stellar physics but also for fields like exoplanet characterization and galactic archaeology. In addition, accretion can alter the surface chemical composition, especially if the accreted material differs in abundance from that of the protostar (Kunitomo and Guillot 2021). This has important implications for interpreting observed stellar abundances and for modeling chemical mixing processes.

Finally, accretion history plays a critical role in understanding young stellar clusters. It can influence the shape of the initial mass function, contribute to the observed luminosity spread among cluster members, and affect the positioning of stars on theoretical isochrones (Baraffe et al. 2009, 2012; Hosokawa et al. 2011). Accurate modeling of accretion is therefore important for interpreting observed features of young clusters.

In this project, I investigate the impact of accretion on stellar structure and evolution using the Cesam2k20 version of the 1D stellar evolution code *Code d'Évolution Stellaire Adaptatif et Modulaire* (CESAM; Marques et al. 2013; Morel 1997; Morel and Lebreton 2008). The goal is to implement accretion in Cesam2k20 in order to study its influence on stellar evolution and internal structure, and to compare the results with theoretical predictions and previous studies using other stellar evolution models, such as MESA (Kunitomo et al. 2017) and STAREVOL (Amard and Matt 2023).

This study focuses on the later stages of the accretion process, after the formation of the second hydrostatic core. I restrict my analysis to low-mass stars, as the accretion process in high-mass stars remains more uncertain and lies beyond the scope of this work.

In the next section, I review the current understanding of pre-main sequence accretion, including the mechanisms of magnetospheric accretion and a brief overview of the observational evidence supporting it. Sec. 3 presents the fundamental equations governing stellar structure and outlines how pre-main sequence evolution is modeled in stellar evolution codes. In Sec. 4, I begin by discussing the modeling of the consequences of accretion, followed by a description of the Cesam2k20 code, including its numerical structure and input physics. I then detail the implementation of accretion in the code. The results of my models are presented in Sec. 5, where I explore the effects of different accretion rates and deuterium abundances, and compare our findings with previous work by Palla and Stahler (1993). Finally, Sec. 6 summarizes our main findings, discusses the limitations of the current work, and outlines future prospects.

2 Pre-main sequence magnetospheric accretion

In this section, I will review the current understanding of stellar accretion, including the mechanisms of magnetospheric accretion and its observational signatures. I first introduce the magnetospheric accretion paradigm, which underpins the interpretation of the observational evidence discussed in the following subsection.

2.1 Magnetospheric accretion paradigm

Stellar magnetic fields play a crucial role in the accretion of pre-main sequence stars, through the mechanism known as magnetospheric accretion (See, for example, Hartmann et al. 2016, for a review). Fig. 1 is a schematic illustration of magnetospheric accretion

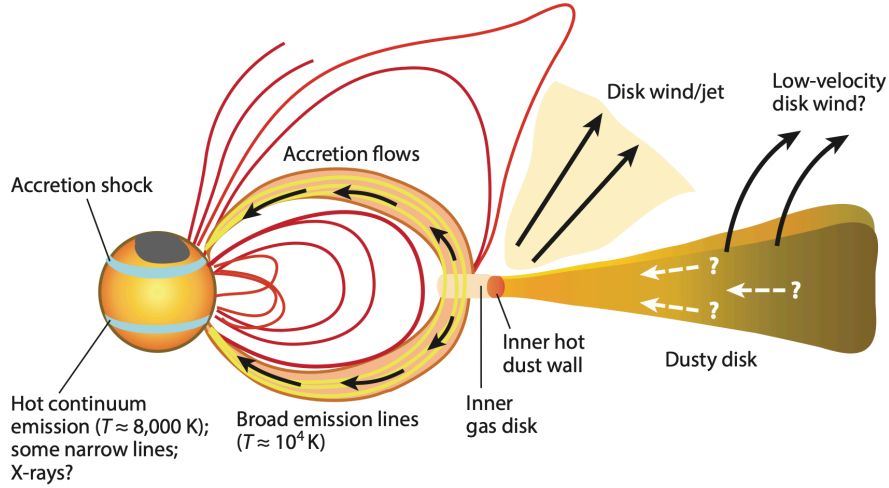


Figure 1: Schematic illustration of magnetospheric accretion onto young low-mass stars. The figure is reproduced from Fig. 1 of Hartmann et al. (2016). See main text for details.

onto young ($1 \lesssim t \lesssim 10$, Myr), low-mass ($\lesssim 1M_{\odot}$) stars. The strong stellar magnetic field truncates the circumstellar disk at a few stellar radii. The dust disk is truncated slightly farther out than the gas disk, as dust in the inner disk sublimates due to heating by the stellar radiation field. The inner edge of the dust disk is responsible for most of the observed near-IR excess. Material from the disk is funneled onto the star along the magnetic field lines, where it is heated to approximately 10^4 K, producing broad emission lines. The accretion flow is accelerated along the field lines, eventually reaching the stellar surface at nearly free-fall velocity. This process leads to the formation of an accretion shock at the stellar surface, where the gas is briefly halted and heated to very high temperatures, emitting X-rays. Most of these X-rays are absorbed and reradiated in the ultraviolet and optical continuum.

Despite recent advances in the study of magnetospheric accretion, many aspects are still under debate. Bouvier (2014) summarizes several open issues regarding the physics of the magnetospheric accretion and ejection processes. One of the long-standing problems is the evolution of stellar rotation: while the angular momentum carried by accreting material should spin up the star, observations reveal that the rotation rates of PMS stars are lower than expected. This discrepancy suggests that some form of magnetic braking must be at work to regulate stellar spin (e.g., Herbst et al. 2007).

Magnetohydrodynamic simulations suggest that jets, disk winds, and magnetospheric ejections are involved in removing angular momentum during accretion (e.g., Ireland et al. 2020; Lii et al. 2014; Romanova et al. 2004). However, the relative importance of these mechanisms in shaping the angular momentum evolution remains under investigation (e.g., Kunitomo et al. 2017). Although the models presented in this work do not include magnetic fields or rotation, understanding the broader framework of magnetospheric accretion is essential for interpreting how accretion affects stellar structure. Including these physical processes for more realistic accretion modeling will be an important direction for future work.

2.2 Observational evidence of magnetospheric accretion

Observations of CTTs provide strong evidence for magnetospheric accretion, including the presence of strong stellar magnetic fields, an inner cavity of a few stellar radii within the magnetosphere, magnetic accretion columns filled with free-falling plasma,

and accretion shocks at the stellar surface.

The accretion shock produces emission in the ultraviolet, optical, and near-infrared wavelengths, as well as a modest amount of X-rays. These emissions serve as crucial diagnostics of the accretion region, allowing measurements of the accretion luminosity which, when combined with stellar mass and radius, provide estimates of accretion rates. Soft X-ray emission, unique to accreting stars, has also been detected from CTTs and is likely produced in the post-shock region (e.g., Kastner et al. 2002). Magnetospheric accretion flows can be identified by redshifted absorption features in specific spectral lines (Muzerolle et al. 2001), while blueshifted forbidden emission lines have been linked to strong winds and mass outflows (e.g., Bally 2016).

Magnetospheric accretion paradigm assumes that the stellar magnetic field is strong enough to counteract the pressure of the accretion disk and disrupt the disk before it reaches the stellar surface (e.g., Koenigl 1991). At the truncation radius R_{trunc} , the magnetic pressure approximately balances the gas ram pressure, i.e., $B^2/8\pi \simeq \frac{1}{2}\rho v^2$, where the relevant velocity is roughly the Keplerian velocity, $v = \sqrt{GM_\star/R_{\text{trunc}}}$. The exact location of this truncation radius will also depend on the accretion rate (see Eq. 2.2 in Bouvier et al. 2007). This framework generally aligns with the measured magnetic field strengths of CTTs, which typically range from a few hundred Gauss to a few kiloGauss (Alencar et al. 2012; Bouvier et al. 2007).

3 Stellar evolution modeling

Stellar evolution modeling involves combining physical principles with numerical methods to simulate how stars change over time. This section first introduces the fundamental equations that describe stellar evolution and then turns the focus to the modeling of pre-main sequence stars.

3.1 Stellar structure equations

Modeling stellar evolution involves defining initial conditions and solving the differential equations that govern the physical processes inside a star, thereby predicting how stellar properties change over time. The primary factors determining an isolated star's evolution are its mass and initial chemical composition. Once specified, these initial parameters are input into the stellar structure equations, which express the physical quantities as functions of position and time (\vec{r}, t). By assuming spherical symmetry, the position can be reduced to the radial distance r from the center, so physical quantities become functions of radius and time, i.e., (r, t) .

Throughout most of stellar evolution, the total stellar mass remains nearly constant except in cases of significant mass loss. In contrast, the stellar radius can vary rapidly as the star passes through different stages. Because Lagrangian coordinates move with the fluid elements, it is more convenient to use the mass coordinate m , defined as the total mass enclosed within radius r , rather than the radius itself. This approach allows us to track the evolution of specific mass shells as they move and change, making it a more natural choice for describing properties such as energy production, chemical composition and angular momentum within the stellar interior.

In the mass coordinate, the system of 1D stellar structure equations can be written as

(See, for example, Kippenhahn et al. 2013):

$$\frac{\partial p}{\partial m} = -\frac{Gm}{4\pi r^2}, \quad (1a)$$

$$\frac{\partial T}{\partial m} = \frac{\partial p}{\partial m} \frac{T}{p} \nabla, \quad (1b)$$

$$\frac{\partial r}{\partial m} = \frac{1}{4\pi r^2 \rho}, \quad (1c)$$

$$\frac{\partial l}{\partial m} = \epsilon_{\text{nuc}} - \epsilon_{\nu} + \epsilon_g, \quad (1d)$$

$$\frac{\partial X_i}{\partial t} = -\frac{\partial F_i}{\partial m} + \Psi_i(p, T, \mathbf{X}), 1 \leq i \leq n_{\text{elem}}, \quad (1e)$$

where G is the gravitational constant, $\nabla \equiv \partial \ln T / \partial \ln p$ is the temperature gradient, ρ is the density, and ϵ_{nuc} , ϵ_{ν} , and ϵ_g are the rates of nuclear energy production, neutrino energy loss, and gravitational energy production, respectively, all expressed in units of power per unit mass. By definition, $\epsilon_{\nu} > 0$. X_i is the abundance of the chemical element i , F_i is the flux of the chemical element i due to diffusion, $\mathbf{X} \equiv \{X_i\}$ is the chemical composition vector, Ψ_i is the rate of change of X_i by thermonuclear reactions, and n_{elem} is the total number of chemical species considered. All quantities (p , l , ρ , T , ϵ , ϵ_{ν} , etc.) are evaluated locally at each stellar layer.

Eq. (1a) describes the hydrostatic equilibrium and Eq. (1c) describes the mass continuity. Eq. (1d) and Eq. (1b) describe the energy production and energy transport, respectively. These equations illustrate a close coupling between stellar structure and the process of energy production and transport. In most stars, energy is primarily transported by radiation and convection, and the value of ∇ depends on the dominant mechanism of energy transport. Eq. (1e) describes the evolution of the chemical composition of the star, which is governed by the nuclear reactions occurring in the star and the transport of chemical elements. This set of equations assumes spherical symmetry and does not account for magnetic fields nor rotation. These are common simplifications in 1D stellar models and are sufficient for many evolutionary studies.

Stellar evolution is typically treated as a one-dimensional boundary value problem with initial conditions given by the initial mass and chemical composition of the star. The boundary conditions are set at the center and surface of the star. Spherical symmetry requires that the radius, luminosity, and chemical element fluxes vanish at the center of the star. Therefore, it is imposed that:

$$r(0, t) = 0, l(0, t) = 0, F_i(0, t) = 0, i = 1, \dots, n_{\text{elem}}. \quad (2)$$

At the surface, the pressure and temperature are set to the values at the base of the stellar atmosphere:

$$p(M_{\star}, t) = p_{\text{atm}}(L_{\star}, R_{\star}, t), T(M_{\star}, t) = T_{\text{atm}}(L_{\star}, R_{\star}, t), \quad (3)$$

where M_{\star} , L_{\star} , and R_{\star} are the stellar mass, luminosity, and radius, respectively. The values of p_{atm} and T_{atm} are derived from reconstruction of the stellar atmosphere, which typically uses empirical relations. As this project focuses on internal structure, I will not delve into the specifics of atmospheric modeling.

With both central and surface boundary conditions specified, and the evolution equations defined in Lagrangian coordinates, the stellar structure problem becomes a well-posed initial-boundary value problem. This framework serves as the basis for numerical

stellar evolution codes, which solve these equations to track the stellar evolution over time.

The solutions to the stellar structure equations yield key observable properties of stars, most notably their luminosity L and effective surface temperature T_{eff} . These two parameters define a star’s position on the Hertzsprung-Russell (HR) diagram, a fundamental tool in astrophysics to understand and visualize stellar evolution. The HR diagram helps to reveal distinct evolutionary stages such as the pre-main sequence, main sequence, and giant branch, offering a simple way to compare models with observations.

However, translating the underlying physics into stellar models is a complex task. In practice, stellar evolution codes can differ substantially in their model initialization methods. These differences can lead to notable variations during the early evolutionary stages, which will be discussed in the Sec. 3.2. Furthermore, differences in formulations, assumptions, and adopted physical ingredients, such as the Equation of State (EoS) and opacities, can substantially influence the predicted stellar properties, often resulting in discrepancies between models. Therefore, it is essential to carefully consider the specific implementations and assumptions of each code when interpreting stellar evolution results. One of the goals of this project is to benchmark our accretion models against those implemented in other stellar evolution codes. The details of our physical inputs will be discussed in Sec. 4.2.

3.2 Pre-main sequence evolution

3.2.1 Pre-main sequence evolution with constant mass

Classically, the modeling of PMS evolution begins with a fully convective star of large radius and luminosity. As the star contracts under gravity, the release of gravitational energy heats the stellar interior. This contraction continues until the central temperature becomes high enough to slow down the contraction and trigger the formation of a radiative core.

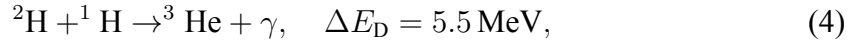
The initial phase of PMS evolution is characterized by a rapid decrease in both radius and luminosity, while the effective temperature remains nearly constant. This phase, known as the Hayashi track (Hayashi 1961), defines the locus in the HR diagram of fully convective stars of a given mass and composition. Energy transport is dominated by convection during this phase. The precise location and slope of the Hayashi track is also sensitive to the treatment of convection, typically modeled using the mixing-length theory (Cox and Giuli 1968). As the star contracts, its internal temperature rises, leading to a quick increase in the opacity of the stellar matter, since at this temperature range the opacity κ scales steeply with temperature, $\kappa \sim T^9$ (Maeder 2009). This, in turn, limits the temperature increase. This feedback mechanism maintains the effective temperature approximately constant, so the star evolve with decreasing radius but a constant effective temperature. As a result, the Hayashi tracks appear on the far right of the HR diagram and follow a steep, nearly vertical path.

The Hayashi track ends at a minimum luminosity, where the central temperature becomes sufficiently high to cause a significant decrease in opacity in the stellar interior. As a result, radiative energy transport becomes more efficient, and a radiative core begins to develop. The star then evolves toward higher effective temperatures while its luminosity remains approximately constant. This marks the beginning of the second phase of PMS evolution, where the star follows a more horizontal path in the HR diagram, known as the Henyey track, first described by Henyey et al. (1955). During this stage, the star evolves with a radiative core while maintaining a convective envelope.

This classic two-phase PMS evolution—first descending the vertical Hayashi track, then moving leftwards on the more horizontal Henyey track—is illustrated in Fig. 2, which shows evolutionary tracks for Cesam2k20 models with masses between 1 and 5, M_{\odot} , assuming initial composition $X \simeq 0.73$, $Y \simeq 0.25$ (see Sec. 4.2 for details of the input physics). Arrows indicate the direction of stellar evolution, with mass labels marking the ends of each track. The nearly vertical portion corresponds to fully convective contraction (Hayashi track), while the more horizontal portion marks the emergence of a radiative core (Henyey track)..

During PMS evolution, gravitational contraction remains the primary energy source, as the central temperature has not yet reached the threshold for hydrogen fusion. However, light elements such as deuterium and lithium can be burned at relatively low temperatures (Kippenhahn et al. 2013).

Deuterium burning is particularly important in PMS evolution, proceeding via the reaction:



which ignites at central temperature of $T_c \sim 10^6$, K.

Lithium burning, involving the dominant isotope ${}^7\text{Li}$, occurs via the reaction:



which sets in at $T_c \sim 2.5 \times 10^6$, K. Although lithium burning releases significantly more energy per reaction than deuterium burning, the former makes little contribution to the total energy production in PMS stars, as lithium is around 10^3 less abundant than deuterium (Grevesse and Sauval 1998).

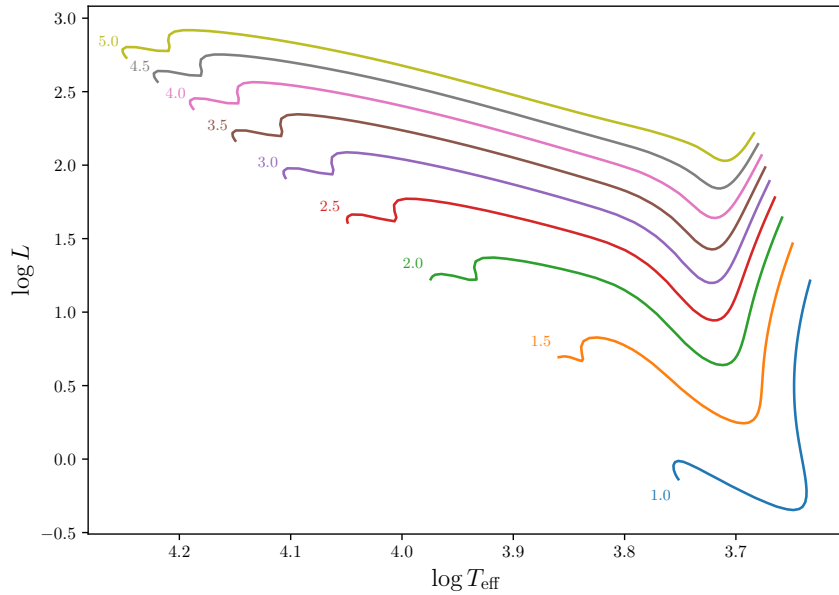


Figure 2: Classic pre-main sequence evolutionary tracks for Cesam2k20 models with masses between 1 and 5, M_{\odot} in the HR diagram. Arrows indicate the direction of stellar evolution, with stellar masses in solar masses labeled at the end of each track. The nearly vertical Hayashi track corresponds to fully convective contraction, while the more horizontal Henyey track marks the phase when contraction slows down and a radiative core develops.

The star is considered to have reached the main sequence once hydrogen fusion becomes the dominant source of energy production, at a central temperature of $T_c \sim 10^7$ K. This beginning of main sequence evolution is referred to as the Zero-Age Main Sequence (ZAMS). From the ZAMS onward, the star’s position in the HR diagram changes relatively slowly during the long phase of central hydrogen burning.

3.2.2 Pre-main sequence evolution with accretion

The classic PMS evolution described above assumes that the star has already acquired its final mass at the beginning of contraction. However, as the observational evidence discussed in Sec. 2.2 indicates, many young stars continue to accrete material from their surrounding environment during the PMS phase. These stars experience a period of relaxation and thermal re-adjustment as they contract, before eventually settling onto a track that closely follows the constant-mass evolution (Kippenhahn et al. 2013).

One physical quantity of importance in this context is the mass accretion rate \dot{M}_{acc} , defined as the rate at which mass is transferred from the surrounding cloud to the proto-star. Estimates of \dot{M}_{acc} are often uncertain by factors of a few, due to their sensitivity to stellar parameters and extinction. These values are typically calculated from the accretion luminosity L_{acc} via:

$$L_{\text{acc}} = \frac{GM_{\star}\dot{M}_{\text{acc}}}{R_{\star}} \left(1 - \frac{R_{\star}}{R_{\text{trunc}}}\right), \quad (6)$$

assuming the material falls freely from the truncation radius R_{trunc} to the stellar surface at radius R_{\star} , (see review by Hartmann et al. 2016).

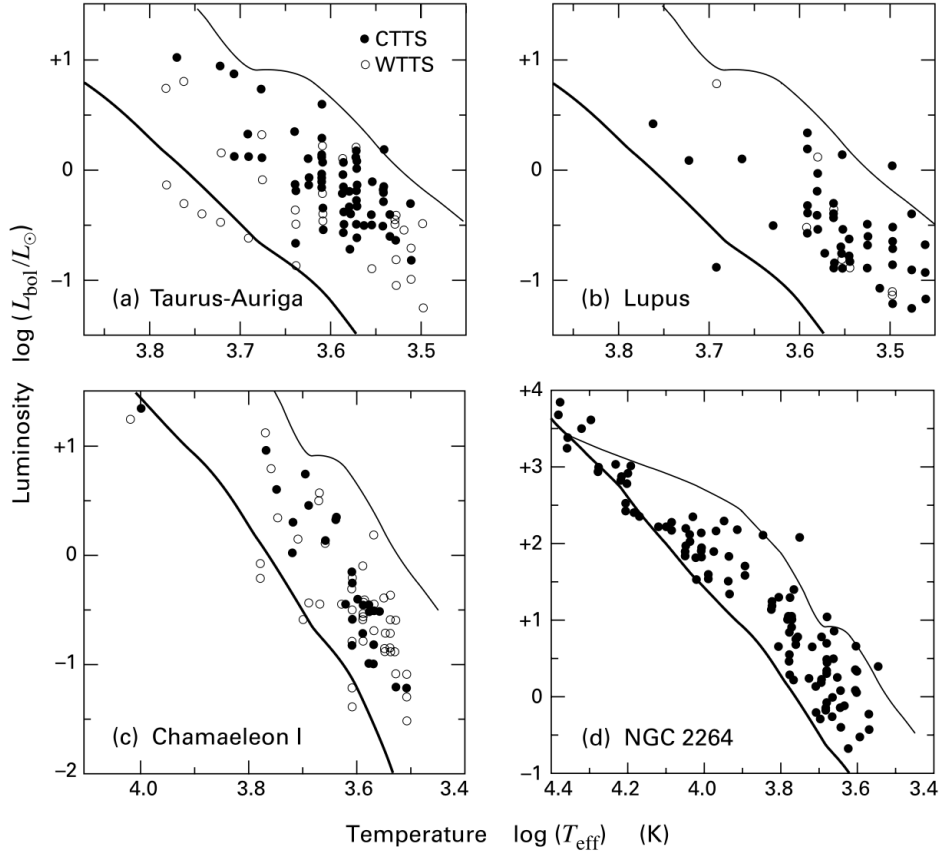


Figure 3: HR diagrams for four star forming regions. In panels (a)-(c), closed circles represent CTTSs, while open circles are WTTSs. In panel (d), the sample includes CTTSs, Herbig Ae/Be stars, and main sequence objects. The thin upper curves are the theoretical birthlines; the thick lower curves are the ZAMS. Reproduced from Fig. 4.9 of Stahler and Palla (2004).

Observational studies reveal a correlation between accretion rates and stellar mass, with more massive stars accreting at higher rates (e.g., Lanzafame et al. 2023; Manara et al. 2017; Muzerolle et al. 2003; Rugel et al. 2018). Models of viscous disk evolution predict a declining \dot{M}_{acc} with stellar age as the circumstellar disk becomes depleted (e.g.,

Gorti and Hollenbach 2009; Hartmann et al. 1998). Despite this, the precise functional form of the mass and time dependence remains under debate. For this study, a constant accretion rate \dot{M}_{acc} is adopted for simplicity.

Deuterium plays a more prominent role in accreting PMS stars than in non-accreting ones, as the accretion flow continuously supplies fresh deuterium. In contrast, non-accreting stars can deplete their initial deuterium rapidly. This deuterium contributes to energy generation through nuclear burning at a rate given by

$$\epsilon_{\text{D}} = [\text{D}/\text{H}] \epsilon_{\text{D},0} \left(\frac{\rho}{1 \text{ g cm}^{-3}} \right) \left(\frac{T}{10^6 \text{ K}} \right)^{n_{\text{D}}}, \quad (7)$$

where $\epsilon_{\text{D},0} = 4.19 \times 10^7 \text{ erg g}^{-1} \text{ s}^{-1}$, $n_{\text{D}} = 11.8$, and $[\text{D}/\text{H}]$ is the number abundance of deuterium relative to hydrogen, i.e., the ratio of deuterium nuclei to hydrogen nuclei in the environment (cf. Eq. 11.27 in Stahler and Palla 2004).

The amount of deuterium in the accreted material can strongly influence PMS evolution. A high deuterium abundance provides more nuclear energy during accretion, leading to greater stellar expansion, while a lower abundance results in a more compact star throughout its evolution toward the main sequence (Kunitomo et al. 2017).

When the main accretion phase ends, the circumstellar disk has mostly been dissipated and become optically thin, allowing the star to appear as a visible object. The locus in the HR diagram where PMS stars of different masses first become visible is known as the birthline (Stahler 1983). Its position is sensitive to the star’s accretion history, initial mass, and chemical composition.

Theoretical birthlines can be compared with observations of TTSSs to evaluate models of PMS evolution. Moreover, the birthline provides insights into the environments in which stars are formed. In Fig. 3, observations of four star forming regions with active star formation are plotted alongside the theoretical birthline and the ZAMS. Stars located below the birthline have recently dispersed their circumstellar envelopes, whereas younger, still-embedded stars cannot yet be placed on the HR diagram due to difficulties in measuring their effective temperatures.

4 Methods

4.1 The consequences of accretion

The most direct consequence of accretion onto a star is the increase in its mass. However, accretion also alters the stellar environment and affects the star’s bolometric luminosity by delivering additional energy. It can also supply fresh deuterium, which contributes significantly to the star’s energy budget through nuclear burning.

As discussed in Sec. 2.1, accretion is a highly complex process involving various physical mechanisms, such as angular momentum transport from the disk to the star, magnetic fields, and outflows like jets and winds. To make the problem tractable in the context of stellar evolution, some simplifications are necessary. In this section, I describe how the consequences of accretion are incorporated into stellar evolution models, focusing on the treatment of gravitational energy, deuterium from accreted material, and the regimes of hot and cold accretion.

Before moving into more details, it is important to note that gravitational energy associated with accretion comes from two distinct sources:

1. work: the gravitational energy released (or absorbed) by the star due to contraction or expansion during its evolution, and

2. heat and radiation: the gravitational potential energy of the material as it falls onto the star, which is partly converted into the thermal energy of the accreted material before it reaches the stellar surface.

The former affects the internal energy budget of the star itself, while the latter relates to how the infalling material delivers its energy upon impact, which depends on the nature of the accretion process (see Sec. 4.1.4).

4.1.1 Gravitational energy

The gravitational energy released during the PMS phase contributes significantly to the stellar energy budget and must be properly accounted for in stellar evolution models. In this section, I describe how this energy is treated in the stellar structure equations, and in the following section, I discuss the specific treatment of gravitational energy associated with accreted material.

The rate of gravitational energy release per unit mass is given by:

$$\epsilon_g = -T \left. \frac{\partial s}{\partial t} \right|_m, \quad (8)$$

where s is the specific entropy.

From the first law of thermodynamics, $dq = du + p dv$, where u is the specific internal energy and $v = 1/\rho$ is the specific volume, one can write:

$$T \left. \frac{\partial s}{\partial t} \right|_m = \left. \frac{\partial q}{\partial t} \right|_m = \left. \frac{\partial u}{\partial t} \right|_m + p \left. \frac{\partial v}{\partial t} \right|_m = \left. \frac{\partial u}{\partial t} \right|_m - \frac{p}{\rho^2} \left. \frac{\partial \rho}{\partial t} \right|_m. \quad (9)$$

In practice, the internal energy depends on the chemical composition and the EoS, which complicates the calculation. However, for a chemically homogeneous star, we can use the Kippenhahn approximation (Kippenhahn et al. 2013), which instead expresses the entropy change as:

$$T \left. \frac{\partial s}{\partial t} \right|_m \simeq c_p \left. \frac{\partial T}{\partial t} \right|_m - \frac{\delta}{\rho} \left. \frac{\partial p}{\partial t} \right|_m, \quad (10)$$

where c_p is the specific heat at constant pressure and $\delta = -(\partial \ln \rho / \partial \ln T)_p$. Since PMS stars are generally fully convective, chemical mixing is highly efficient throughout the interior, which makes the Kippenhahn approximation appropriate in this context of this project.

Substituting the Kippenhahn approximation into the energy conservation equation, Eq. (1d) becomes:

$$\frac{\partial l}{\partial m} = \epsilon_{\text{nuc}} - \epsilon_\nu - c_p \left. \frac{\partial T}{\partial t} \right|_m + \frac{\delta}{\rho} \left. \frac{\partial p}{\partial t} \right|_m. \quad (11)$$

However, applying Eq. (11) to evolving stellar models with accretion presents a complication: the computation of time derivatives at a given mass requires knowledge of the thermodynamic and chemical properties of the accreted material, which are not directly available from the stellar model. Estimating these properties requires special treatment, which is addressed in the next two sections.

4.1.2 Coordinate transformation for accretion modeling

To incorporate accreted mass into the stellar model, its thermal and compositional properties must be specified. A common simplification for the thermal structure is to

assume that the accreted material is homologous to the stellar surface—that is, it shares the same entropy. This assumption is justified by comparing characteristic timescales. The thermal timescale of a mass element, $\tau_{\text{th}} \simeq \Delta m c_p T / L$, describes how quickly it reaches thermal equilibrium with its surroundings. The accretion timescale, $\tau_{\text{acc}} \simeq \Delta m / \dot{M}_{\text{acc}}$, is the time over which the mass is accreted. When $\tau_{\text{th}} \ll \tau_{\text{acc}}$, the accreted material has time to thermally equilibrate with the stellar surface, thereby justifying the use of the homologous assumption. This condition is equivalent to $\dot{M}_{\text{acc}} c_p T \ll L$, which is typically satisfied near the stellar surface (Paxton et al. 2015; Sugimoto and Nomoto 1975).

The homologous assumption permits the use of fractional mass coordinates, defined as (Sugimoto and Nomoto 1975)

$$q_m = \frac{m}{M_\star}, \quad (12)$$

to describe the geometry of the star.

Switching from the Lagrangian mass coordinate m to the fractional mass coordinate q_m modifies the form of time derivatives in the structure equations. For a generic function $f(m, t)$, the total differential can be expressed both in terms of m and q_m :

$$df = \left. \frac{\partial f}{\partial t} \right|_{q_m} dt + \left. \frac{\partial f}{\partial q_m} \right|_t dq_m \quad (13)$$

$$= \left. \frac{\partial f}{\partial t} \right|_{q_m} dt + \left. \frac{\partial f}{\partial q_m} \right|_t \left(\left. \frac{\partial q_m}{\partial t} \right|_m dt + \left. \frac{\partial q_m}{\partial m} \right|_t dm \right),$$

$$df = \left. \frac{\partial f}{\partial t} \right|_m dt + \left. \frac{\partial f}{\partial m} \right|_t dm \quad (14)$$

Equating the two expressions yields:

$$\left. \frac{\partial f}{\partial t} \right|_m = \left. \frac{\partial f}{\partial t} \right|_{q_m} + \left. \frac{\partial f}{\partial q_m} \right|_t \left. \frac{\partial q_m}{\partial t} \right|_m \quad (15)$$

$$\left. \frac{\partial f}{\partial m} \right|_t = \left. \frac{\partial f}{\partial q_m} \right|_t \left. \frac{\partial q_m}{\partial m} \right|_t. \quad (16)$$

Using this, Eq. (8) can be rewritten in terms of q_m as:

$$\epsilon_g = -T \left. \frac{\partial s}{\partial t} \right|_{q_m} - T \left. \frac{\partial s}{\partial q_m} \right|_t \left. \frac{\partial q_m}{\partial t} \right|_m. \quad (17)$$

While the expressions for ϵ_g in Eq. (8) and its reformulation above are mathematically equivalent, the latter is more convenient when the time derivative at fixed mass coordinate is not readily available.

4.1.3 Deuterium from the accreted material

In contrast to the thermal properties, the chemical composition of the accreted material is not necessarily homologous to that of the stellar surface. In particular, the deuterium content of the accreted gas can differ significantly from that of the star. This difference arises because deuterium burning becomes extremely efficient once the central temperature exceeds a critical threshold $T_c \gtrsim 10^6$ K. Since PMS stars are generally fully convective, efficient mixing ensures that the entire interior remains chemically homogeneous. As a result, deuterium can be depleted as fast as it is supplied, leaving the stellar interior nearly devoid of it, even while fresh deuterium continues to arrive from the surrounding environment.

The amount of deuterium in the accreted material can significantly affect the evolution of PMS stars (e.g., Amard and Matt 2023; Kunitomo et al. 2017). Deuterium burning provides a substantial amount of energy that can halt or even reverse the star’s contraction, thereby influencing both its radius and luminosity. In this sense, deuterium acts as a thermostat: because the nuclear energy generation rate ϵ_D is highly sensitive to temperature (as seen in the exponent $n_D = 11.8$ in Eq. (7)), a rise in central temperature dramatically increases ϵ_D , causing the star to expand. This expansion reduces the central temperature, which in turn suppresses the burning rate (Stahler and Palla 2004)—a self-regulating feedback mechanism.

This thermostatic behavior can only be sustained if deuterium is replenished at a sufficient rate. At steady-state burning, the deuterium luminosity can be approximated as:

$$L_D \equiv \int_0^{M_*} \epsilon_D dm \simeq \dot{M}_{\text{acc}} \delta, \quad (18)$$

where δ is the energy available from deuterium per gram of accreted material:

$$\delta = \frac{[\text{D}/\text{H}] X \Delta E_D}{m_H}. \quad (19)$$

Here, $X \sim 0.73$ is the hydrogen mass fraction, $\Delta E_D = 5.5 \text{ MeV}$ is the energy released per deuterium fusion reaction, and m_H is the mass of a hydrogen atom.

The deuterium-to-hydrogen ratio, $[\text{D}/\text{H}]$, in the accreted material is typically assumed to match that of the interstellar medium (ISM). However, its precise value remains uncertain. Observations of the local ISM suggest a wide range of values, from $0.98 \pm 0.38 \times 10^{-5}$ (Hébrard et al. 2005) to at least $2.13 \pm 0.24 \times 10^{-5}$ (Linsky et al. 2006). Moreover, $[\text{D}/\text{H}]_{\text{ISM}}$ is expected to evolve over time, since estimates of the primordial deuterium abundance, $[\text{D}/\text{H}]_{\text{prim}} \sim 2.5 \times 10^{-5}$, are higher than those observed in the local ISM (e.g., Prantzos 2007). As shown by Kunitomo and Guillot (2021), the deuterium content in the accretion disk may also evolve over time due to the formation and growth of planetesimals, further complicating the picture.

Due to these complications, in this study I do not account for the time evolution of $[\text{D}/\text{H}]$. Instead, I adopt a fixed value of $[\text{D}/\text{H}] = 2.0 \times 10^{-5}$ for the accreting models and explore variations in this parameter to assess its impact on the evolution of PMS stars.

4.1.4 Hot and cold accretion

As material accretes onto a PMS star, a portion of its gravitational energy is converted into internal energy, either through work or heat, while the remainder is radiated away. How much of this energy is deposited into the star depends strongly on the nature of the accretion process. Two main factors influence the efficiency of energy deposition:

1. the geometry of the accretion flow (e.g., spherical or disk-like), and
2. the radiative losses at the accretion shock and the stellar surface.

The geometry of the accretion flow influences the energy of the material as it arrives at the stellar surface. Each unit mass of accreted gas initially possesses a gravitational potential energy of $-GM_*/R_*$. During its infall onto the star, part of this energy is converted into macroscopic kinetic energy and radiation, which is then transferred to the star as work or heat when the gas hits the stellar surface. The fraction of energy deposited into the star can be expressed as $\beta GM_*/R_*$, where the factor β characterizes the physical nature of the accretion flow. For example, for gravitationally bound material, $\beta \leq 1$, while

for thin-disk accretion from the equatorial region, typical values are $\beta \leq 0.5$ (Hartmann et al. 1998; Prialnik and Livio 1985).

The fractional surface area covered by accretion shock can influence the radiative efficiency, as the shocked region and the stellar photosphere have different radiative properties. Let f_{shock} denote the fraction of the stellar surface covered by the shock. The shocked area emits an accretion luminosity $L_{\text{acc}} = 4\pi R_{\star}^2 f_{\text{shock}} F_{\text{acc}}$, where F_{acc} is the mean radiative flux over the accreting region. Meanwhile, the remaining stellar surface radiates at the star's intrinsic luminosity, $L_{\text{photo}} = 4\pi R_{\star}^2 (1 - f_{\text{shock}}) T_{\text{eff}}^4$. The total losses from the shock and the photosphere counteract the energy injection from the accreted material.

Following the simplified treatment by Hartmann et al. (1998), these considerations can be combined into an effective energy injection rate from the accreted material:

$$L_{\text{add}} = \xi_{\text{add}} \frac{GM_{\star} \dot{M}_{\text{acc}}}{R_{\star}}, \quad (20)$$

where ξ_{add}^1 is a dimensionless parameter to quantify the fraction of energy injected by the accreted material into the star. The value of ξ_{add} depends on both factors mentioned above. Radiative transfer calculations by Stahler et al. (1980) show that $\xi_{\text{add}} \leq 3/4$, while for disk accretion the upper limit is typically $\xi_{\text{add}} \simeq 0.5$. This value can be further reduced by stellar rotation, which converts some of the accretion energy into rotational energy (Kunitomo et al. 2017). The case of $\xi_{\text{add}} = 0.5$ is referred to as hot accretion, while $\xi_{\text{add}} = 0$ is referred to as cold accretion, where no heat is injected into the stellar interior (though the added mass and entropy still modify the star's hydrostatic equilibrium).

This heat injection can affect the evolution of accreting stars (e.g., Amard and Matt 2023; Kunitomo et al. 2017). A higher value of ξ_{add} causes the star to expand by adding thermal energy. However, for simplicity, heat injection during accretion is not included in this work. By neglecting this effect, I am effectively considering the case where $\xi_{\text{add}} = 0$, which is a reasonable approximation for most PMS stars, as the majority of the accretion energy is expected to be radiated away before reaching the star (Hartmann et al. 1998).

4.2 The stellar evolution code Cesam2k20

We use the stellar evolution code Cesam2k20 (Marques et al. 2013; Morel 1997; Morel and Lebreton 2008) to model stellar evolution with accretion. Cesam2k20 is an open-source, one-dimensional stellar evolution code (available at the [Cesam2k20 website](#)) that employs a spectral method to solve the stellar structure equations given in Eqns. (1). To our knowledge, it is the only stellar evolution code that utilizes a spectral method, which offers the advantages of superconvergence and high numerical precision compared to the more commonly used finite-difference methods in stellar evolution modeling. The following subsections describe its numerical implementation, including the choice of variables, automatic grid-point allocation, the formulation of the structure equations, and the adopted input physics.

4.2.1 Lagrangian variables

The system of equations in Eqns. (1) encapsulates the fundamental physics governing stellar structure and evolution. However, in numerical implementation, these equations are often reformulated to improve stability and convergence. One effective approach,

¹My ξ_{add} is equivalent to α in Eq. (5) of Hartmann et al. (1998).

discussed by Morel (1997), is to use the set of variables introduced by Eggleton (1971),

$$\left(\frac{m}{M_\odot}\right)^{2/3}, \quad \left(\frac{r}{R_\odot}\right)^2, \quad \left(\frac{l}{L_\odot}\right)^{2/3}, \quad l \geq 0$$

This choice improves numerical precision and helps avoid singularities at the stellar center. In cases where $l < 0$ —which can occur during late evolutionary stages—the variable l/L_\odot is used instead. Since this project focuses on the pre-main sequence phase, where such cases do not arise, we adopt the Eggleton variables throughout.

Additionally, because pressure and temperature can span several orders of magnitude in the stellar interior, it is numerically advantageous to work with their logarithms. Accordingly, the set of variables ultimately used in *Cesam2k20* is:

$$\xi = \ln p, \quad \eta = \ln T, \quad \zeta = \left(\frac{r}{R_\odot}\right)^2, \quad \lambda = \left(\frac{l}{L_\odot}\right)^{2/3}, \quad \mu = \left(\frac{m}{M_\odot}\right)^{2/3}. \quad (21)$$

4.2.2 Automatic location of grid points

To resolve the large variations in physical quantities during stellar evolution, an adaptive grid is necessary. To achieve automatic allocation, *Cesam2k20* uses a strictly monotonic spacing function, $Q(\mu, t)$, to distribute grid points based on local physical conditions. Grid points are placed such that the difference in $Q(\mu, t)$ between adjacent points is equal to a time-dependent spacing function $\psi(t)$ (Eggleton 1971; Morel 1997; Press et al. 1992).

Formally, at each time step t , the grid points μ_i , $i = 1, \dots, n$ are allocated such that:

$$Q(\mu_{i+1}, t) - Q(\mu_i, t) = \psi(t), \quad i = 1, \dots, n-1, \quad (22)$$

where $\psi(t)$ is determined during the numerical integration.

The default form of the spacing function $Q(\mu, t)$ used in *Cesam2k20* is:

$$Q(\mu, t) = (-1)\xi + (0)\eta + (0)\zeta + (0)\lambda + (15)\mu, \quad (23)$$

where the values in parentheses serve as weights for each variable in the calculation of the distance between grid points. See Manchon (2021) and Morel (1997) for the rationale behind this choice. These coefficients can be adjusted in the numerical settings to achieve higher resolution in specific variables if desired. The dependence of $Q(\mu, t)$ on pressure (ξ) and mass (μ) ensures finer resolution in regions of steep pressure and density gradients. In the core, where the pressure gradient is modest, resolution is primarily controlled by mass change; while in the outer envelope, where pressure varies rapidly, the grid is refined mostly based on pressure changes.

To map physical coordinates onto the numerical grid, *Cesam2k20* defines an index function $q(\mu, t)$ that takes integer values from 1 to n at the grid points. Values of physical variables at positions between grid points are obtained by interpolation on the grid. The derivative of Q with respect to this index gives:

$$\left.\frac{\partial Q}{\partial q}\right|_t = \left.\frac{\partial Q}{\partial \mu}\right|_t \left.\frac{\partial \mu}{\partial q}\right|_t = \theta(\mu, t) \left.\frac{\partial \mu}{\partial q}\right|_t = \psi(t), \quad (24)$$

where $\theta(\mu, t)$ is directly obtained from the analytic form of $Q(\mu, t)$ in Eq. (23).

The introduction of $\psi(t)$ and $\theta(\mu, t)$ requires two additional equations for closure:

$$\frac{\partial \mu}{\partial q} = \frac{\psi}{\theta}, \quad \frac{\partial \psi}{\partial q} = 0. \quad (25)$$

The first equation relates the mass coordinate to grid index, while the second enforces constant spacing in Q -space. This approach enables efficient resolution of the stellar structure, especially during rapid evolutionary phases.

4.2.3 Structure equations

With the variables introduced in Secs. 4.2.1 and 4.2.2, the stellar structure equations can be expressed in a form more suitable for integration on an equidistant grid in the numerical index $q_i = 1, \dots, n$.

The full set of structure and composition equations solved at each time step is:

$$0 = \frac{\partial \xi}{\partial q} - \left[-\frac{3G}{8\pi} \left(\frac{M_\odot}{R_\odot} \right)^2 \left(\frac{\mu}{\zeta} \right)^2 \right] e^{-\xi} \frac{\psi}{\theta}, \quad (26a)$$

$$0 = \frac{\partial \eta}{\partial q} - \left[-\frac{3G}{8\pi} \left(\frac{M_\odot}{R_\odot} \right)^2 \left(\frac{\mu}{\zeta} \right)^2 \right] e^{-\xi} \frac{\psi}{\theta} \nabla, \quad (26b)$$

$$0 = \frac{\partial \zeta}{\partial q} - \frac{3}{4\pi} \frac{M_\odot}{R_\odot^3} \frac{1}{\rho} \left(\frac{\mu}{\zeta} \right)^{1/2} \frac{\psi}{\theta}, \quad (26c)$$

$$0 = \frac{\partial \lambda}{\partial q} - \frac{M_\odot}{L_\odot} \left(\frac{\mu}{\lambda} \right)^{1/2} (\epsilon - \epsilon_\nu + \epsilon_g) \frac{\psi}{\theta}, \quad (26d)$$

$$0 = \frac{\partial \mu}{\partial q} - \frac{\psi}{\theta}, \quad (26e)$$

$$0 = \frac{\partial \psi}{\partial q}, \quad (26f)$$

$$0 = \frac{\partial X_i}{\partial t} + \frac{2}{3M_\odot \mu^{1/2}} \frac{\partial F_i}{\partial \mu} - \Psi_i(\xi, \eta, \mathbf{X}), 1 \leq i \leq n_{\text{elem}}. \quad (26g)$$

These equations are solved simultaneously with boundary conditions-at the center:

$$\zeta(1, t) = 0, \quad \lambda(1, t) = 0, \quad \mu(1, t) = 0, \quad (27)$$

and at the surface:

$$\xi(n, t) = \xi_{\text{atm}}(L_\star, R_\star, t), \quad \eta(n, t) = \eta_{\text{atm}}(L_\star, R_\star, t), \quad \mu(n, t) = \mu_{\text{atm}}, \quad (28)$$

along with constitutive relations (e.g., equations of state, opacity laws) to evolve the stellar model in time.

4.2.4 PMS initial models

At time $t = 0$, to begin the computation, the values of pressure $p(m, 0)$, temperature $T(m, 0)$, radius $r(m, 0)$, luminosity $l(m, 0)$, and chemical abundances $\mathbf{X}(m, 0)$ must be specified for $m \in [0, M_\star(t = 0)]$. In *Cesam2k20*, these values are taken from precomputed tables of a homogeneous PMS stellar model. *Cesam2k20* also has the capacity to start from a ZAMS initial model, or continue the evolution of a previous model. However, for the purpose of this project, I need to start from a PMS model, therefore I will not go into the details of these two other methods of initialization.

This initialization method from a PMS model is based on the work of Iben (1965). At the zero-age of the PMS phase, the star's only energy source is gravitational contraction, with no contribution from nuclear burning or neutrino losses, i.e., $\epsilon = 0$ and $\epsilon_\nu = 0$. Furthermore, the star is fully convective, so it has a constant entropy profile throughout its interior, except in the thin superadiabatic layers near the surface (*ibid.*). In this regime, the energy equation (Eq. (1d)) simplifies to:

$$\frac{\partial l}{\partial m} = \epsilon_g = -T \frac{\partial s}{\partial t} = cT, \quad (29)$$

where c is a contraction constant, with units of $L_{\odot} M_{\odot}^{-1} \text{K}^{-1}$, characteristic of a fully convective star in quasi-equilibrium. Varying the value of c shifts the starting point of the star's evolution track in the HR diagram.

The Iben method proceeds by constructing two PMS models, labeled #1 and #2, with the same mass M_{\star} , but slightly different contraction constants c_1 and c_2 . These models should be close enough that the change in gravitational energy between them approximates the radiative energy loss over a time step Δt :

$$\frac{L_1 + L_2}{2} \Delta t \sim \left(\frac{GM^2}{R_2} - \frac{GM^2}{R_1} \right), \quad (30)$$

where L_1, R_1 and L_2, R_2 are the luminosities and radii of models #1 and #2, respectively (cf. Eq. (13) Morel 1997). Evolution can then proceed using model #2 and time step Δt .

In Cesam2k20, the user provides an input value $c_1 = c_{\text{iben}}$, the Iben constant, and the code sets $c_2 = 1.1 c_1$. The appropriate range of values for c_{iben} depends on the stellar mass. At fixed mass, a lower Iben constant leads to lower luminosity and a higher central temperature. For example, $c_{\text{iben}} = 0.02$ yields $T_c \sim 10^5 \text{K}$, while smaller values such as $c_{\text{iben}} = 0.005$ and $c_{\text{iben}} = 0.00008$ correspond to $T_c \sim 5 \times 10^5 \text{K}$ and 10^6K , respectively. Although these values are similar in order of magnitude across different stellar masses, each mass range requires its own acceptable interval of c_{iben} values to ensure convergence to a valid PMS model.

In this project, I focus on the evolution of the second hydrostatic core, whose mass is on the order of a Jovian mass, $M_{\text{Jup}} \sim 10^{-3} M_{\odot}$ (e.g., Vaytet et al. 2013). Previous studies, such as Kunitomo et al. (2017) and Amard and Matt (2023), have used a fiducial initial mass of $M_{\text{seed}} = 0.01 M_{\odot}$, which is slightly larger than the typical second core mass derived from radiative hydrodynamic simulations. One of the key challenges in modeling the second hydrostatic core is its very low temperature, where the standard EoS for stellar matter no longer applies. Due to the limitations in the available EoS tables implemented in Cesam2k20, I choose to initialize my models with a higher seed mass of $M_{\text{seed}} = 0.1 M_{\odot}$. Additionally, I compute initial models with $M_{\text{seed}} = 1 M_{\odot}$ to compare with the results of Palla and Stahler (1993). I acknowledge that this choice is not ideal, but it is the best compromise given the constraints of the code and the available EoS. This study primarily focuses on modeling the accretion process, while the incorporation of a more realistic initial seed mass is deferred to future work.

4.2.5 Input physics

Although Cesam2k20 is capable of modeling rotation and diffusion, I keep the input physics simple at this stage to focus on the impact of accretion on stellar structure. The interactions of accretion with rotation and diffusion will be an important aspect in future work. The models are computed for 1D, single stars without rotation, magnetic fields, or diffusion. Mass loss is not considered; the only mechanism that alters the stellar mass is accretion. The initial chemical composition follows the solar mixture of Asplund et al. (2009), with meteoritic determination for non-volatile elements as recommended by Serenelli et al. (2009). The isotopic ratios follow the solar composition by Asplund et al. (2021), except for the deuterium abundance, which is varied to explore its impact on accreting stars.

Convection is modeled using the mixing-length theory (MLT; Cox and Giuli 1968), which describes convective energy transport occurs via the motion of fluid elements over a characteristic distance, the mixing length, before dissolving into their surroundings. This length is typically taken to be proportional to the pressure scale height. This proportionality is set by the mixing-length parameter, α_{MLT} . We adopt a solar-calibrated value of

Parameter Type	Description
Mass	accretion + no mass loss
Chemical composition	AGS09+S10
Convection	MLT + No overshoot
Diffusion	None
EoS	OPAL2005
Opacity	OPAL and AF
Nuclear reaction	NACRE + LUNA
Atmosphere	Hopf, $\tau_{\max} = 20.0$

Table 1: Summary of input parameters for Cesam2k20 models; refer to the text for more details.

$\alpha_{\text{MLT}} = 1.64$. Convective boundaries are determined using the Schwarzschild criterion, with no convective overshooting.

The EoS and opacity are interpolated from the OPAL2005 tables (Iglesias and Rogers 1996; Rogers and Nayfonov 2002; Rogers and Iglesias 1992), and supplemented at low temperatures by the AF opacity tables (Ferguson et al. 2005). Nuclear reaction rates are based on NACRE (Aikawa et al. 2006) and LUNA (Broggini et al. 2018) tables. The models include the full PP and CNO cycles, tracking the evolution of abundances for ^1H , ^2H , ^3He , ^4He , ^7Li , ^7Be , ^{12}C , ^{13}C , ^{14}N , ^{15}N , ^{16}O , and ^{17}O .

Neutrino energy losses are treated using the prescriptions of Haft et al. (1994) for plasma neutrinos and Weigert (1966) for photoneutrinos. The atmosphere is implemented using a Hopf $T(\tau)$ relation from Hubeny and Mihalas (2015), with the base of the atmosphere set at an optical depth of $\tau_{\max} = 20$, where the solution of the internal structure equations is matched to that of the atmosphere model.

The input physics are summarized in Table 1. Building on this framework, I next describe the implementation of accretion in Cesam2k20.

4.3 Accretion in Cesam2k20

Building on the general modeling of accretion described in Sec. 4.1 and the details of the stellar evolution code Cesam2k20 in Sec. 4.2, this section outlines how key physical effects—particularly the treatment of gravitational energy and deuterium from accreted material—are implemented within the code.

4.3.1 Homologous coordinates for Cesam2k20

Since Cesam2k20 uses dimensionless Eggleton variable $\mu \equiv (m/M_{\odot})^{2/3}$ as the mass coordinate, the homologous coordinate defined in Eq. (12) need to be adapted accordingly. Consider two stellar models: one at the previous time step with mass M_1 , and another at the current time step with mass $M_2 = M_1 + \dot{M}_{\text{acc}}dt$, where dt is small. The goal is to choose a coordinate such that the thermodynamic properties of the accreted material can be retrieved from those of the surface in the previous model.

I define the homologous coordinate as:

$$\mu_x \equiv \left(\frac{m}{M_{\star}} \right)^{2/3}, \quad (31)$$

where M_{\star} is either M_1 or M_2 , depending on whether the quantity is evaluated at the previous or current time step.

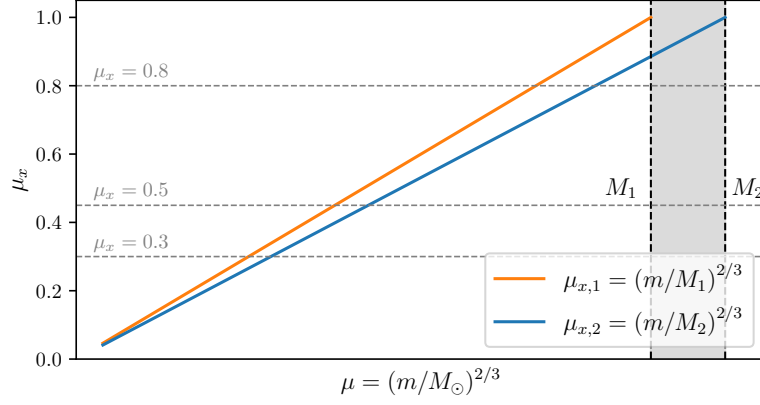


Figure 4: Scheme of the mapping between homologous coordinates μ_x and Lagrangian coordinates μ in Cesam2k20. Mass shells at the same μ correspond to different μ_x values as the total stellar mass increases from M_1 to M_2 . The two vertical black dashed lines mark M_1 and M_2 . The gray shaded region highlights the newly accreted material whose thermodynamic properties can be retrieved via this mapping. The difference in total mass between the two models is exaggerated for clarity.

Then the time derivative $(\partial q_m / \partial t)_m$ in Eq. (15), with μ_x replaced by q_m and m replaced by μ , evaluates to:

$$\left. \frac{\partial \mu_x}{\partial t} \right|_{\mu} = \mu \frac{\partial (M_{\odot} / M_2)^{2/3}}{\partial t} = -\frac{2}{3} \mu \frac{M_{\odot}^{2/3}}{M_2^{5/3}} \dot{M}_{\text{acc}} = -\frac{2}{3} \mu_x \frac{\dot{M}_{\text{acc}}}{M_2}, \quad (32)$$

where μ_x is substituted by $\mu (M_{\odot} / M_2)^{2/3}$.

The relation between the two coordinates, $(\partial q_m / \partial m)_t$ in Eq. (16), is more straightforward:

$$\left. \frac{\partial \mu_x}{\partial \mu} \right|_t = \left(\frac{M_{\odot}}{M_2} \right)^{2/3}. \quad (33)$$

These expressions will be useful later for computing the structure equation Eq. (26d) and its partial derivatives in the next section.

To map thermodynamic quantities from the previous to the current model, a table of physical variables as functions of $\mu_{x,1} = \mu_1 \left(\frac{M_{\odot}}{M_1} \right)^{2/3}$ is constructed at the previous time step. At the current time step, for each grid point μ_2 , the corresponding homologous coordinate $\mu_{x,2} = \mu_2 \left(\frac{M_{\odot}}{M_2} \right)^{2/3}$ is computed, and the thermodynamic properties are obtained by interpolating values stored in the table at this $\mu_{x,2}$.

This mapping is illustrated in Fig. 4, which shows how mass shells at the same μ correspond to different μ_x values as the total stellar mass increases from M_1 to M_2 . This procedure assumes that thermal properties remain identical at fixed μ_x between time steps, so the accreted material inherits the thermodynamic state of the surface layers from the previous model. The rest of the computation proceeds using the set of Eggleton variables defined in Eq. (21).

4.3.2 Modifications to the structure equations

In Cesam2k20, the nonlinear boundary value problem is solved using the Newton-Raphson method (Press et al. 1992). In the context of stellar evolution modeling, this approach is commonly known as the Henyey method (Henyey et al. 1959). The structure

equations are solved iteratively, with the Jacobian matrix of the system in Eqns. (26a)-(26g) updated at each iteration. This matrix contains the partial derivatives of the structure equations with respect to the variables ξ , η , ζ , λ , and μ , which guide the solution toward convergence. Following the standard Henyey scheme, each time step is split into two substeps: first, the chemical composition is updated while the structural variables (ξ , η , ζ , λ , and μ) are held fixed; second, the structure is recomputed to restore quasi-static equilibrium with the updated composition. I focus here on the modifications introduced in the quasi-static equilibrium step, and discuss changes to the treatment of chemical evolution in the next section.

The principal modifications introduced in this work concern the energy equation, Eq. (26d), specifically the gravitational energy generation term, ϵ_g . This term is revised to include the gravitational energy contributed by accreted material. Consequently, the corresponding partial derivatives in the Jacobian matrix are recalculated to account for this change.

Using the homologous coordinate μ_x and applying Eq. (16) and Eq. (32), the expression of ϵ_g in Eq. (10) expands to:

$$\begin{aligned} T \frac{\partial s}{\partial t} \Big|_{\mu} &= c_p \frac{\partial T}{\partial t} \Big|_{\mu} - \frac{\delta}{\rho} \frac{\partial p}{\partial t} \Big|_{\mu}, \\ &= c_p \frac{\partial T}{\partial t} \Big|_{\mu_x} - \frac{\delta}{\rho} \frac{\partial p}{\partial t} \Big|_{\mu_x} - \frac{2}{3} \mu \frac{M_{\odot}^{2/3}}{M_2^{5/3}} \dot{M}_{\text{acc}} \frac{\partial \mu}{\partial \mu_x} \Big|_t \left(c_p \frac{\partial T}{\partial \mu} \Big|_t - \frac{\delta}{\rho} \frac{\partial p}{\partial \mu} \Big|_t \right). \end{aligned} \quad (34)$$

It is important to distinguish between spatial and temporal derivatives in this context, as they serve different purposes. Spatial derivatives are evaluated at the current time step using data from the EoS and opacity tables and are used to solve the nonlinear boundary value problem. In contrast, temporal derivatives are involved in the evolution of the system, which is an initial value problem, and require data from the previous time step.

More explicitly, the implementation of Eq. (34) in Cesam2k20 reads:

$$T \frac{\partial s}{\partial t} \Big|_{\mu} = c_p \frac{T_{\mu_x} - T_{\mu_x}^t}{dt} - \frac{\delta}{\rho} \frac{p_{\mu_x} - p_{\mu_x}^t}{dt} - \frac{2}{3} \mu \frac{M_{\odot}^{2/3}}{M_2^{5/3}} \dot{M}_{\text{acc}} \frac{\partial \mu}{\partial \mu_x} \Big|_t \left(c_p \frac{\partial T}{\partial \mu} \Big|_t - \frac{\delta}{\rho} \frac{\partial p}{\partial \mu} \Big|_t \right), \quad (35)$$

where T_{μ_x} and p_{μ_x} are the temperature and pressure at the current time step; $T_{\mu_x}^t$ and $p_{\mu_x}^t$ are those at the previous time step; all quantities are evaluated at the same coordinate μ_x ; and dt is the time interval between the two models.

The next step is to compute the partial derivatives of the gravitational energy generation term, ϵ_g . Due to their complexity and length, the full expressions are provided in Appendix 6. Below is an example derivation of the partial derivative of Eq. (35) with respect to $\xi = \ln P$.

Using Eqns. (26a) and (26b), one can write:

$$\frac{\partial T}{\partial \mu} \Big|_t = e^{\eta} \left[-\frac{3G}{8\pi} \left(\frac{M_{\odot}}{R_{\odot}} \right)^2 \left(\frac{\mu}{\zeta} \right)^2 \right] e^{-\xi} \nabla, \quad (36)$$

$$\frac{\partial p}{\partial \mu} \Big|_t = -\frac{3G}{8\pi} \left(\frac{M_{\odot}}{R_{\odot}} \right)^2 \left(\frac{\mu}{\zeta} \right)^2, \quad (37)$$

which shows that $(\partial T / \partial \mu)_t$ depends on ξ , η , ζ , λ , and μ , while $(\partial p / \partial \mu)_t$ depends only on ζ and μ .

Then,

$$\frac{\partial}{\partial \xi} \frac{\partial T}{\partial \mu} \Big|_t = e^{\eta} \left[-\frac{3G}{8\pi} \left(\frac{M_{\odot}}{R_{\odot}} \right)^2 \left(\frac{\mu}{\zeta} \right)^2 \right] \left(-e^{-\xi} \nabla + e^{-\xi} \frac{\partial \nabla}{\partial \xi} \right), \quad (38)$$

and

$$\left. \frac{\partial}{\partial \xi} \frac{\partial p}{\partial \mu} \right|_t = 0. \quad (39)$$

Canceling the null terms, the full expression for the derivative of $T(\partial s/\partial t)$ with respect to ξ is:

$$\frac{\partial}{\partial \xi} \left(T \frac{\partial s}{\partial t} \right) = \left\{ \frac{\partial c_p}{\partial \xi} (T_{\mu_x} - T_{\mu_x}^t) - \frac{\delta}{\rho} \left[\left(\frac{1}{\delta} \frac{\partial \delta}{\partial \xi} - \frac{1}{\rho^2} \frac{\partial \rho}{\partial \xi} \right) (p_{\mu_x} - p_{\mu_x}^t) + \frac{\partial p_{\mu_x}}{\partial \xi} \right] \right\} \frac{1}{dt} \quad (40)$$

$$- \frac{2}{3} \dot{M}_{\text{acc}} \frac{M_{\odot}^{2/3}}{M_2^{5/3}} \mu \left. \frac{\partial \mu}{\partial \mu_x} \right|_t \left\{ \left. \frac{\partial c_p}{\partial \xi} \frac{\partial T}{\partial \mu} \right|_t + c_p \left. \frac{\partial}{\partial \xi} \frac{\partial T}{\partial \mu} \right|_t - \frac{\delta}{\rho} \left(\frac{1}{\delta} \frac{\partial \delta}{\partial \xi} - \frac{1}{\rho} \frac{\partial \rho}{\partial \xi} \right) \left. \frac{\partial p}{\partial \mu} \right|_t \right\} \quad (41)$$

Partial derivatives with respect to the other variables are derived similarly, completing the necessary modifications to the structure equations.

4.3.3 Adding deuterium to the accreted material

As with thermodynamic properties, the chemical composition of the accreted material must be specified. However, because the accreted composition can differ significantly from that of the star (see Sec. 4.1.3), the homologous assumption used for thermodynamic quantities does not apply. Instead, the accreted material is treated as a separate layer with its own composition.

The chemical composition is stored as a function of the mass coordinate, and chemical transport is computed at the beginning of the each time step. During this computation, composition values at desired locations are obtained by interpolating the tables; when outside the range, the last stored point, i.e., the surface composition is used.

To account for a different composition in the accreted material, at the start of each time step I patch the chemical composition table from the previous step (defined up to mass M_1) to the new total mass M_2 , assigning the additional layers the initial model's composition. This assumes that the initial model has the same composition as its accretion disk, which is generally valid since no thermonuclear reactions have occurred during the formation of the second hydrostatic core. For deuterium, a new free parameter $[D/H]$ is introduced to vary its abundance, and the effects are presented in Sec. 5.4.

5 Results and discussions

5.1 Accreting vs. non-accreting stellar models

The radius evolution and HR diagram of the accreting model are compared with those of a non-accreting model in Fig. 5. The model starts from a seed mass of $0.1 M_{\odot}$ with an Iben constant of $c_{\text{iben}} = 5 \times 10^{-5}$, and accretes up to $1 M_{\odot}$ at a rate of $10^{-5} M_{\odot}/\text{yr}$. It is computed with a deuterium abundance of $[D/H] = 2.0 \times 10^{-5}$. The evolutionary tracks of accreting and classic models diverge significantly during the early stages. The accreting model starts from a lower mass, which leads to a smaller radius, and it undergoes phases of expansion and contraction. In contrast, the non-accreting model contracts continuously until it reaches the main sequence.

The expansion seen in the accreting model is driven by the energy released from burning deuterium contained in the newly accreted material, which is absent in the non-accreting case. When accretion ends, the accreting model converges with the track of the

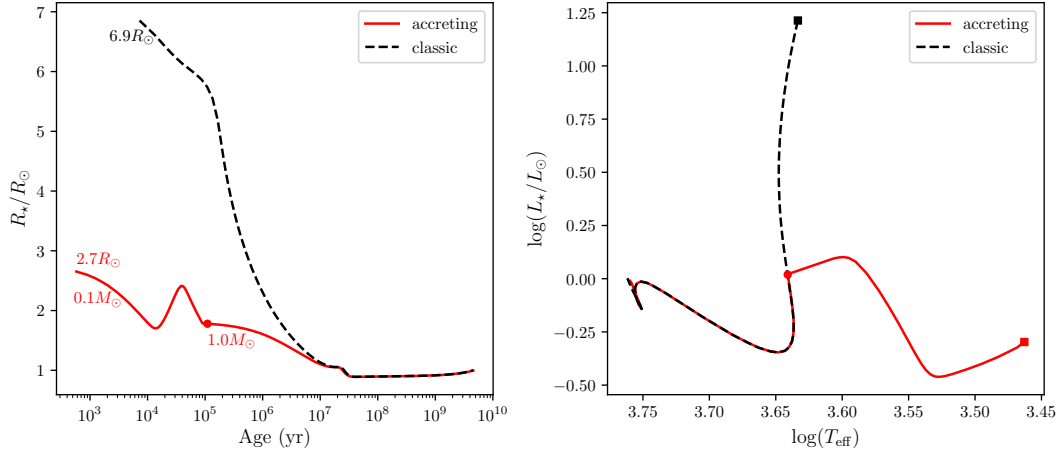


Figure 5: Radius evolution (left panel) and HR diagram (right panel) of accreting and non-accreting stellar models. The accreting model is shown with solid red lines, and the non-accreting model with dashed black lines. Red and black squares indicate the initial locations of each model. The red circle marks the end of accretion in the accreting model. The model starts from a seed mass of $0.1 M_\odot$ with an Iben constant of $c_{\text{iben}} = 5 \times 10^{-5}$, and accretes up to $1 M_\odot$. It is computed with a deuterium abundance of $[D/H] = 2.0 \times 10^{-5}$ and an accretion rate of $10^{-5} M_\odot/\text{yr}$. The non-accreting model has a fixed mass of $1 M_\odot$. Both models stop at ZAMS.

non-accreting one, as shown in the right panel of Fig. 5. In this model, the accretion phase appears to leave little lasting effect on the subsequent evolution. However, this might be due to the relatively large seed mass of $M_{\text{seed}} = 0.1 M_\odot$ adopted here. Previous studies using a lower seed mass $M_{\text{seed}} = 0.01 M_\odot$, such as Kunitomo et al. (2017) and Amard and Matt (2023), the post-accretion evolution can deviate from that of non-accreting stars.

The imprints of accretion on stellar evolution become more pronounced at higher final masses. Fig. 6 compares the evolution of an accreting model with a final mass of $2 M_\odot$ to a non-accreting model of the same mass. The accreting model begins from the same seed mass and follows the same accretion rate and deuterium abundance as in Fig. 5. Unlike the $1 M_\odot$ case, the accreting model does not join directly the non-accreting track after accretion ends but remains slightly lower in luminosity, only approaching the non-accreting track near the ZAMS. This difference is likely due to the larger amount of mass accreted, which amplifies the impact of accretion, and dominates over the initial setup.

To better understand the evolution before the main sequence, Fig. 7 shows the evolution of the radius and mass of the accreting model in Fig. 5, alongside a comparable figure from Kunitomo et al. (2017). Following their classification, I mark five evolution-ary phases:

- (I) the contraction phase, where the star contracts and heats up as it accretes mass;
- (II) the deuterium-burning phase, where the star reaches a central temperature of $\sim 10^6$ K and starts burning deuterium, leading to a rapid expansion;
- (III) the second contraction phase, where the deuterium supply becomes insufficient to maintain the expansion, the energy generation rate drops, and the star begins contracting again until the end of accretion;
- (IV) the swelling phase, where the star expands slightly due to changes in its internal entropy profile; and
- (V) the main sequence, where hydrogen burning begins and the star settles into a long-term stable evolution.

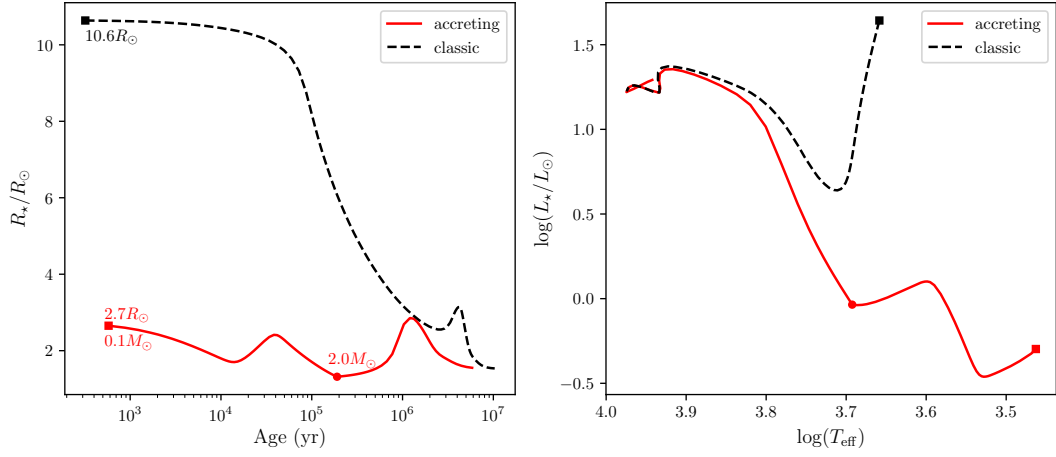


Figure 6: Similar to Fig. 5, but showing an accreting model with a final mass of $2 M_{\odot}$ and a non-accreting model of $2 M_{\odot}$. All other parameters for the accreting model are the same. Both models stop at ZAMS.

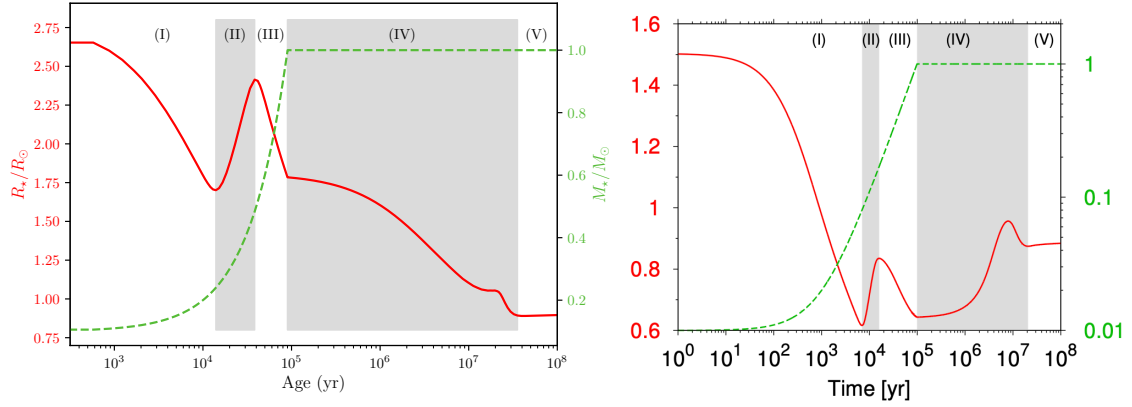


Figure 7: Left panel: Radius (left axis) and mass (right axis) evolution of an accreting model. Right panel: Fig. 1 from Kunitomo et al. (2017), showing a similar plot computed using MESA; the axes are in the same units as in the left panel. The accreting model is the same as in Fig. 5. Radius is shown in red and mass in green. The five evolution phases are labeled as: (I) the contraction phase; (II) deuterium-burning phase; (III) second contraction phase until the end of accretion; (IV) swelling phase; and (V) main sequence. See text for more a detailed description of each phase.

Although I adopt this naming convention, the behavior of my model differs notably in phase (IV). Unlike the swelling seen in Fig. 1 of Kunitomo et al. (2017), my model shows no expansion during this phase. This difference arises because my initial model has a much larger radius, as the seed mass is $0.1 M_{\odot}$ instead of their $0.01 M_{\odot}$, which results in a higher initial entropy. Since the star is already relatively bloated, the entropy redistribution during phase (IV) is insufficient to drive further swelling. This swelling phase is more apparent in the $2 M_{\odot}$ accreting model shown in Fig. 6.

Nonetheless, the deuterium-burning phase (II) exhibits a comparable degree of expansion: in Kunitomo et al. (*ibid.*), the radius increases from ~ 0.6 to $\sim 0.8 R_{\odot}$ (a factor of 1.3), while my model expands from ~ 1.7 to $\sim 2.4 R_{\odot}$, (a factor of 1.4). Similarly, the subsequent contraction (III) reduces the radius in both models to a value slightly above that prior to the deuterium burning phase.

5.2 Dependence on the initial central temperature

The Iben constant c_{iben} controls the initial central temperature of the star, which can significantly influence the PMS evolution. To illustrate this dependence, I compute a set of initial models with different Iben constants: $c_{\text{iben}} = 5 \times 10^{-4}$, 5×10^{-5} , and 1×10^{-5} for stellar masses between 0.5 and $2.5 M_{\odot}$. The results are shown in Fig. 8.

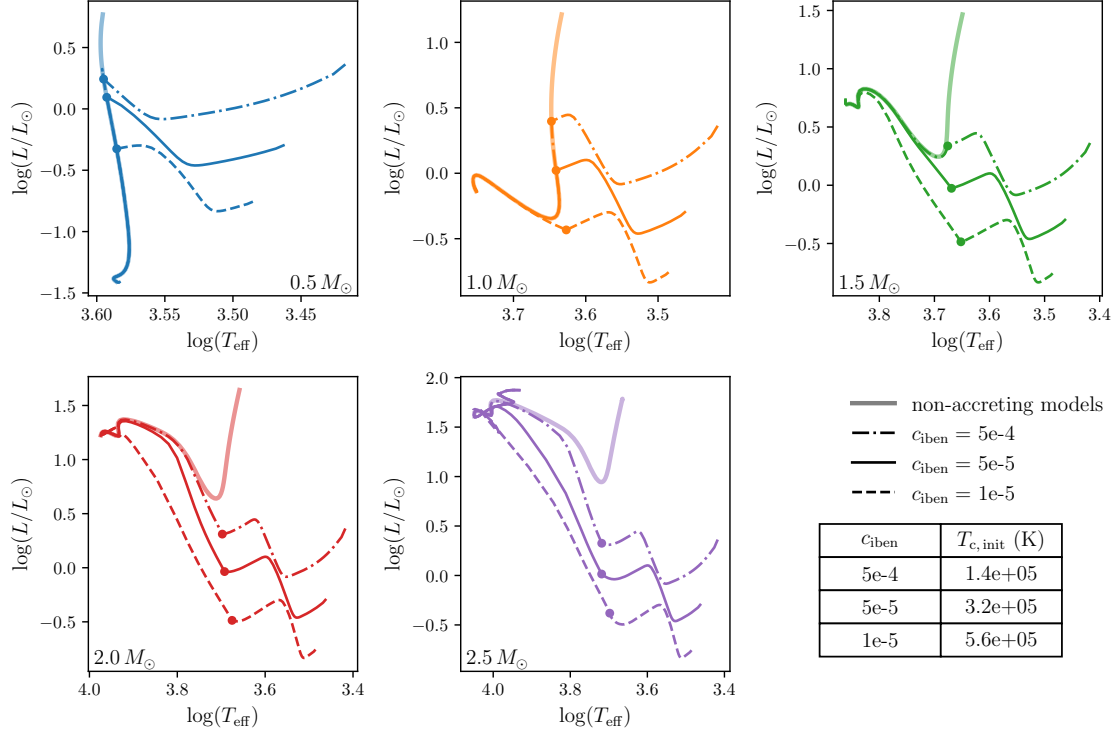


Figure 8: Comparison of initial models computed with different Iben constants using Cesam2k20, for stellar masses between 0.5 and $2.5 M_{\odot}$. Non-accreting (classic) models are shown as faint solid lines for reference. The dot-dashed lines correspond to models with $c_{\text{iben}} = 5 \times 10^{-4}$, the solid lines to models with $c_{\text{iben}} = 5 \times 10^{-5}$, and the dashed lines to models with $c_{\text{iben}} = 1 \times 10^{-5}$. Solid circles mark the moment when accretion is completed. Corresponding initial central temperatures are listed in the table.

The evolutionary tracks differ drastically with varying Iben constants. Models with lower c_{iben} start with lower initial central temperatures and thus begin their evolution from a more luminous positions on the HR diagram, closer to the classical Hayashi and Henyey tracks. Ultimately, the models with the lowest Iben constant (1×10^{-5}) converge with the non-accreting tracks the earliest, whereas those with the highest constant (5×10^{-4}) remain below the non-accreting tracks for stellar masses above $1 M_{\odot}$ for a more extended period, even after accretion ends.

This behavior can be understood by examining the burning plots and central temperature evolution in Fig. 9. Higher initial central temperatures lead to earlier onset of deuterium burning, which causes a greater expansion during the deuterium-burning phase. This expansion lowers the effective temperature, which explains the models' lower position on the HR diagram.

5.3 Dependence on accretion rates

Fig. 10 presents a comparison between models with two different constant accretion rates: $\dot{M}_{\text{acc}} = 10^{-5} M_{\odot}/\text{yr}$ and $10^{-4} M_{\odot}/\text{yr}$. The differences between them are moderate.

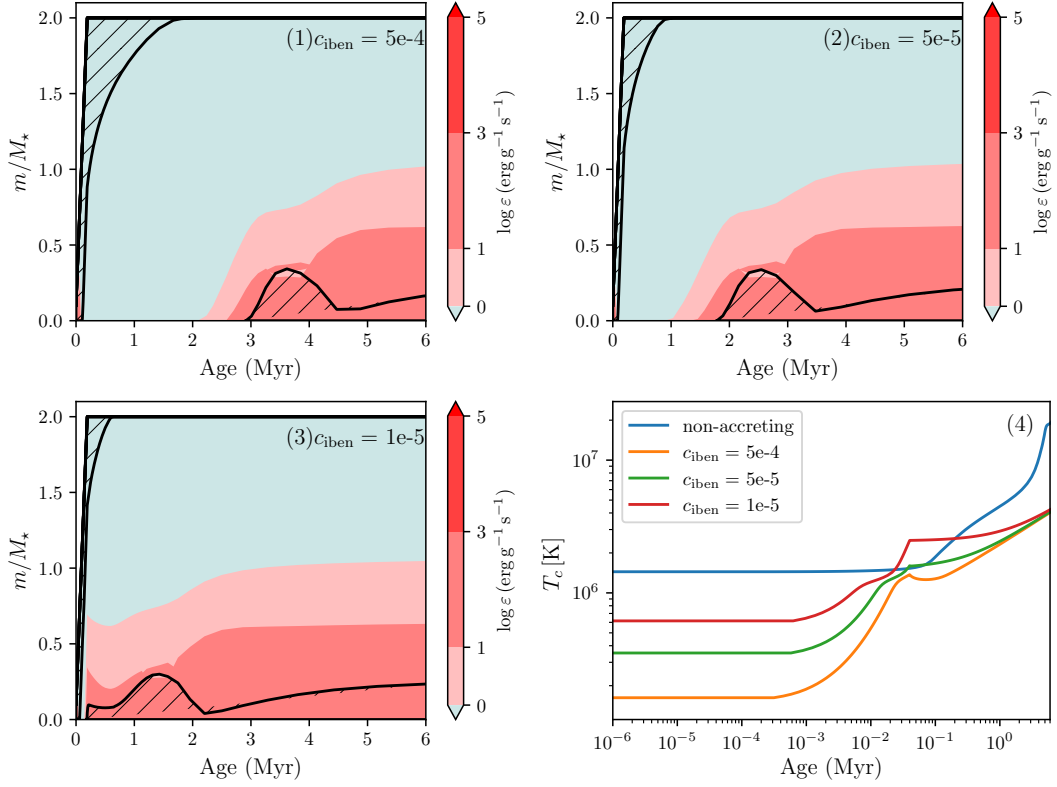


Figure 9: Panels (1)-(3): Burning plots of accreting models with a final mass $M_{\text{final}} = 2 M_{\odot}$, and Iben constants $c_{\text{iben}} = 5 \times 10^{-4}$, 5×10^{-5} , and 1×10^{-5} , respectively. The color scale shows the logarithm of the energy generation rate in $\text{erg g}^{-1} \text{s}^{-1}$. The dashed regions mark convective zones. Panel (4): Central temperature evolution of the non-accreting model and accreting models with different Iben constants. Age is shown on a logarithmic scale to highlight the early evolution.

A higher accretion rate results in slightly higher luminosities, as the increased mass and energy influx accelerates the contraction, thereby raising the central temperature more rapidly. This trend is illustrated more clearly in Fig. 11, which shows the evolution of radius and central temperature for $1.5 M_{\odot}$ models.

These modest differences between different accretion rates are consistent with the findings of Hosokawa et al. (2011) and Kunitomo et al. (2017), who also reported that the accretion rate plays a relatively minor role in determining the overall evolutionary path.

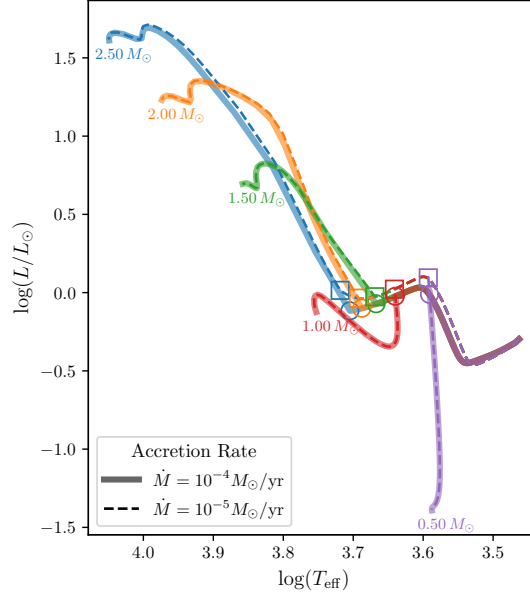


Figure 10: HR diagrams of low-mass accreting models with accretion rates of $10^{-5} M_{\odot}/\text{yr}$ (wide, solid lines) and $10^{-4} M_{\odot}/\text{yr}$ (thin, dashed lines). The models are initialized with a seed mass of $0.1 M_{\odot}$ and a deuterium abundance of $[D/H] = 2.0 \times 10^{-5}$. The open squares and circles indicate the end of the accretion phases, for models with $\dot{M}_{\text{acc}} = 10^{-5} M_{\odot}/\text{yr}$ and $\dot{M}_{\text{acc}} = 10^{-4} M_{\odot}/\text{yr}$, respectively.

5.4 Dependence on deuterium abundance

The deuterium content in the accreted material has a stronger influence on the evolution of accreting protostars than the accretion rate. Fig. 12 compares models with two different deuterium abundances: $[D/H] = 2.0 \times 10^{-5}$ and $[D/H] = 2.5 \times 10^{-5}$. The left panel shows models with an accretion rate of $\dot{M}_{\text{acc}} = 10^{-5} M_{\odot}/\text{yr}$, while the right panel shows models with $\dot{M}_{\text{acc}} = 10^{-4} M_{\odot}/\text{yr}$. The resulting evolution of stellar radius and central temperature for accreting models with final mass $M_{\text{final}} = 2 M_{\odot}$ is shown in Fig. 13.

The contraction phases of the accreting models with different deuterium abundances show no visible difference. However, once deuterium is ignited, the model with higher deuterium abundance expands to a greater extent. This larger radius is maintained during the subsequent second contraction phase and the swelling phase, only disappearing as the star approaches the main sequence. The radius difference is also reflected in the central temperatures (shown on the right axis of Fig. 13): during the deuterium-burning, second contraction, and swelling phases, the model with higher deuterium abundance exhibits lower central temperatures than the model with lower deuterium abundance.

Models with higher deuterium abundances exhibit larger radii and higher luminosities during the early phases of evolution. This behavior stems from the enhanced energy

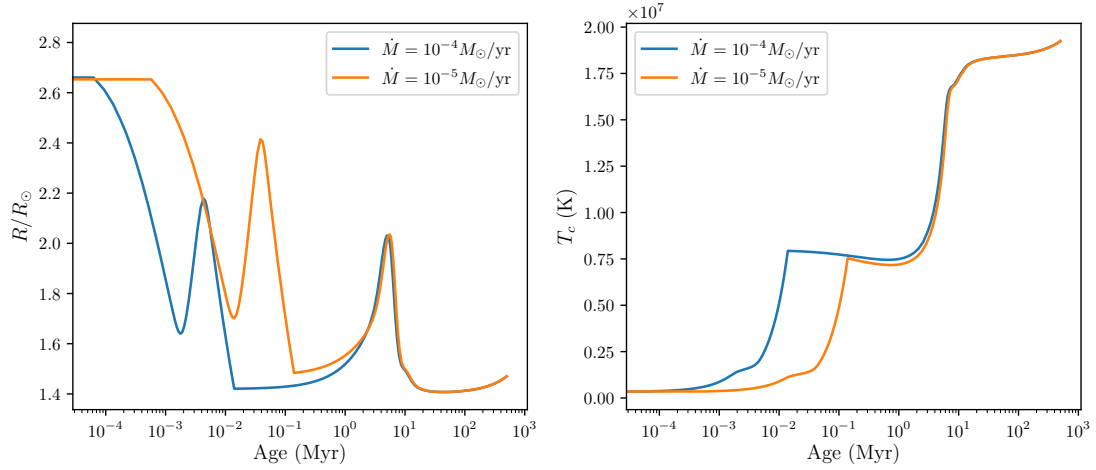


Figure 11: Radius (left panel) and central temperature (right panel) evolution of accreting models of final mass $M_{\text{final}} = 1.5 M_{\odot}$ with different accretion rates. The blue lines correspond to the model with an accretion rate of $10^{-4} M_{\odot}/\text{yr}$, while the orange lines correspond to the model with an accretion rate of $10^{-5} M_{\odot}/\text{yr}$. Both models start from a seed mass of $0.1 M_{\odot}$ and have a deuterium abundance of $[D/H] = 2.0 \times 10^{-5}$.

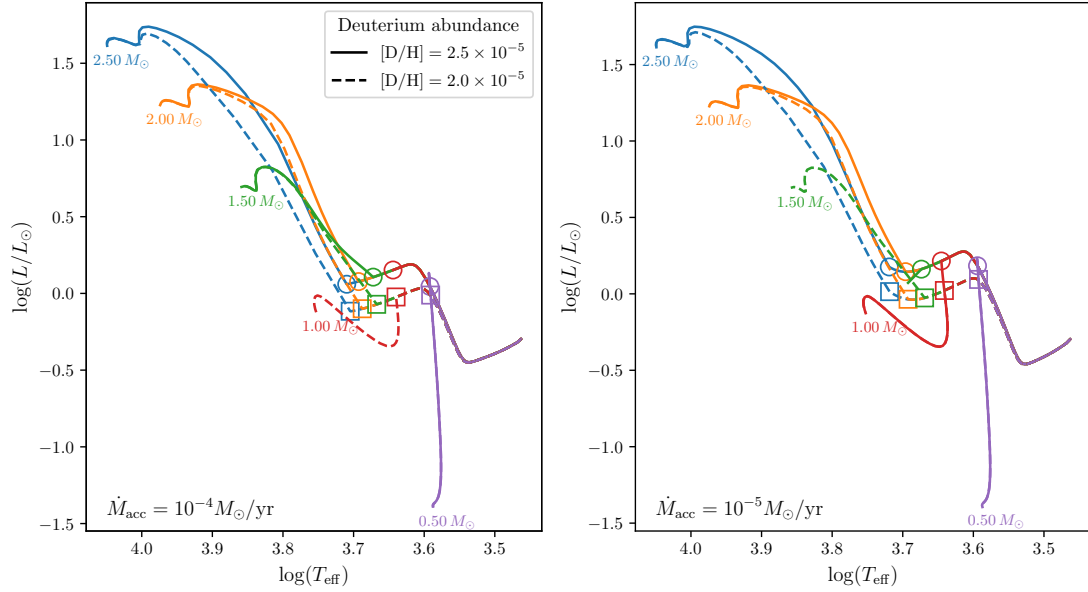


Figure 12: HR diagrams of accreting models with different deuterium abundances in the accreted material. Left panel: models with an accretion rate of $\dot{M}_{\text{acc}} = 10^{-5} M_{\odot}/\text{yr}$. Right panel: models with $\dot{M}_{\text{acc}} = 10^{-4} M_{\odot}/\text{yr}$. Solid and dashed lines correspond to deuterium abundances of 2.5×10^{-5} and 2.0×10^{-5} , respectively. The end of the accretion phase is marked by open circles for higher and open squares for lower deuterium abundances. Two models could not finish due to convergence issues: the $1 M_{\odot}$ model with $\dot{M}_{\text{acc}} = 10^{-5} M_{\odot}/\text{yr}$ and $[D/H] = 2.5 \times 10^{-5}$ (red solid line, left panel); the $1.5 M_{\odot}$ model with $\dot{M}_{\text{acc}} = 10^{-4} M_{\odot}/\text{yr}$ and $[D/H] = 2.5 \times 10^{-5}$ (green solid line, right panel).

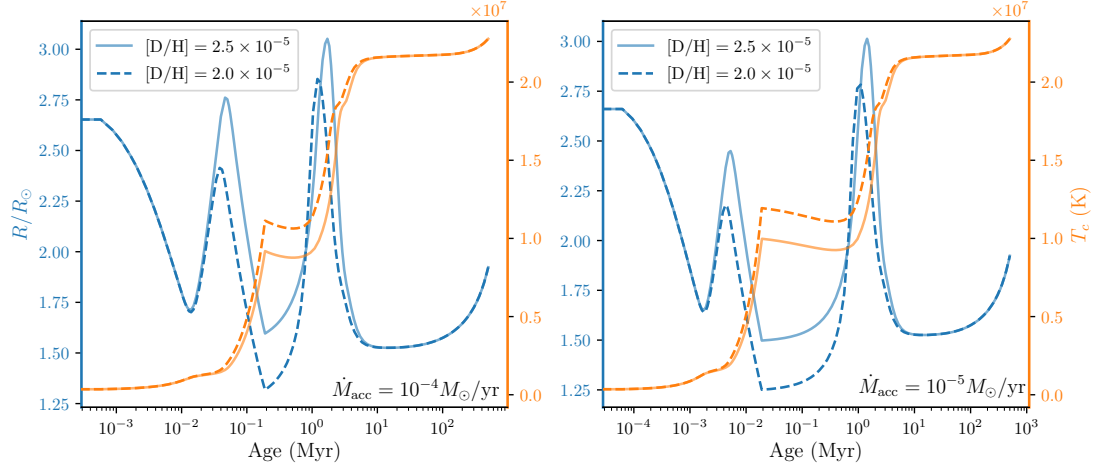


Figure 13: Evolution of stellar radius (R/R_{\odot} , blue) and central temperature (T_c , orange) as a function of age for accreting protostars with final mass $M_{\text{final}} = 2 M_{\odot}$ with two different deuterium abundances: $[D/H] = 2.5 \times 10^{-5}$ (solid lines) and $[D/H] = 2.0 \times 10^{-5}$ (dashed lines). Left panel: models with an accretion rate of $\dot{M}_{\text{acc}} = 10^{-5} M_{\odot}/\text{yr}$. Right panel: models with $\dot{M}_{\text{acc}} = 10^{-4} M_{\odot}/\text{yr}$. Blue and orange curves correspond to stellar radius and central temperature, respectively, plotted on separate y-axes.

production via deuterium burning, which more effectively counteracts gravitational contraction. In contrast, models with lower deuterium abundances contract more rapidly, as indicated by a steeper rise in central temperature in the right axes of Fig. 13. The expansion of radius is more visible in models with higher accretion rates, where the rapid supply of deuterium leads to a higher energy production rate from deuterium burning, more effectively resisting gravitational contraction.

5.5 The birthline

As discussed in Sec. 3.2.2, the birthline serves as a key diagnostic for understanding the early evolution of accreting protostars. In the left panel Fig. 14, I present a reproduction with Cesam2k20 of the birthline originally computed by Palla and Stahler (1993).

To ensure consistency with their setup, I adopt a seed mass of $M_{\text{seed}} = 1 M_{\odot}$ (instead of the $0.1 M_{\odot}$ used elsewhere in this work), an initial central temperature of $T_c \sim 5 \times 10^5 \text{ K}$, and a deuterium abundance of $[D/H] = 2.5 \times 10^{-5}$. These parameters are consistent with those used in their study. The birthline is constructed by identifying the position in the HR diagram where accretion ceases, i.e., where the star reaches its target final mass M_{final} .

Since the publication of Palla and Stahler (ibid.), both observational constraints and stellar modeling techniques have evolved significantly. Consequently, my models differ in several physical ingredients, for example, the equation of state, opacity tables, nuclear reaction rates, and initial chemical composition. These updates lead to some deviations between the two birthlines.

The most noticeable differences appear at the lower-mass end, particularly for the $1.5 M_{\odot}$, $2.0 M_{\odot}$, and $2.5 M_{\odot}$ models, which in my results lie at higher luminosities than in the original Palla and Stahler (ibid.) birthline. This discrepancy likely arises from the relatively small mass difference between the seed and final masses in these models. As discussed in Sec. 5.2, using a larger seed mass in Cesam2k20 tends to shift the early evolutionary track toward higher luminosities in the HR diagram.

To further examine this effect, Fig. 15 presents the radius and central temperature evo-

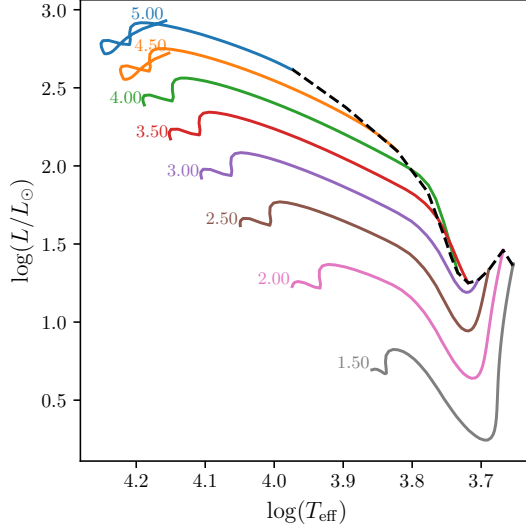


Figure 14: Left panel: HR diagram of accreting stars of different final masses (solid lines) and the birthline (black dashed line), with an accretion rate of $10^{-5} M_{\odot}/\text{yr}$. Right panel: The mass-radius relation. The accreting models start with $M_{\text{seed}} = 1 M_{\odot}$ and $T_c \sim 5 \times 10^5 \text{ K}$. The deuterium abundance is $[D/H] = 2.5 \times 10^{-5}$. Each evolutionary tracks begins at the birthline and terminates at ZAMS.

lution of accreting models with $M_{\text{final}} = 1.5$ to $4.5 M_{\odot}$. Although all models start from the same central temperature, higher-mass models quickly reach higher central temperatures and reach the main sequence earlier, reflecting their more rapid evolution.

6 Conclusion

In this work, I investigated the impact of accretion on the PMS evolution of low-mass protostars using the stellar evolution code *Cesam2k20*. To this end, I implemented accretion in *Cesam2k20* by modifying the structure equations to account for both mass and energy input from the accreted material. A central element of this implementation was a revised treatment of the gravitational energy term in the energy equation, which ensures the energy contribution of the accreted matter is properly included. Additionally, I modified the treatment of chemical composition to incorporate the deuterium abundance in the accreted material, which can differ significantly from that of the protostar.

With accretion implemented, I computed a series of accreting stellar models with varying final masses, accretion rates, and deuterium abundances, and compared their evolution to that of classical non-accreting models. I also reproduced the protostellar birthline originally calculated by Palla and Stahler (1993), using updated input physics.

The main findings of this study can be summarized as follows:

Accreting vs. non-accreting models: Accreting protostars follow markedly different evolutionary tracks from non-accreting stars, particularly during the early stages. While non-accreting models undergo monotonic gravitational contraction, accreting protostars undergo alternating phases of expansion and contraction due to the interplay between gravitation and the counteracting effects of deuterium burning and changes in internal entropy. The choice of seed mass also affects the evolution: my models, initialized with higher seed masses ($0.1 M_{\odot}$), start with more entropy and larger radii, likely contributing to differences in the swelling phase relative to previous studies using smaller seed masses ($0.01 M_{\odot}$).

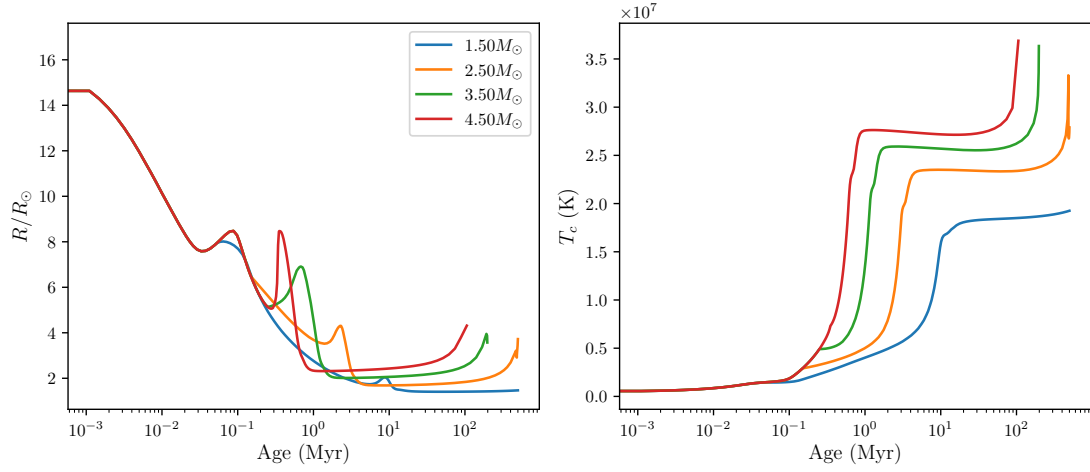


Figure 15: Radius (left panel) and central temperature (right panel) evolution for accreting proto-stars from $M_{\text{seed}} = 1 M_\odot$ to final mass $M_{\text{final}} = 1.5 - 4.5 M_\odot$ with an accretion rate of $\dot{M}_{\text{acc}} = 10^{-5} M_\odot/\text{yr}$. The models are computed with a deuterium abundance of $[\text{D}/\text{H}] = 2.0 \times 10^{-5}$.

Dependence on initial central temperature: The initial central temperature, controlled by the Iben constant, significantly affects early evolution. Models with higher Iben constants begin with lower central temperatures and larger radii, placing them closer to the classical Hayashi or Henyey tracks on the HR diagram. In contrast, models with lower Iben constants start with higher central temperatures, allowing them to ignite deuterium earlier and undergo more pronounced expansion during the deuterium-burning phase. Models with higher Iben constants approach the non-accreting tracks sooner, while those with lower constants remain below the non-accreting tracks for a longer period.

Dependence on accretion rate: The accretion rate has a relatively minor impact on the evolutionary track. Models with higher accretion rates exhibit slightly higher luminosities and smaller radii, as the increased mass and energy influx accelerate the contraction and raise the central temperature more rapidly. However, the differences are not as significant as those arising from variations in deuterium abundance or initial central temperature.

Dependence on deuterium abundance: The deuterium abundance in the accreted material strongly influences protostellar evolution. Higher deuterium abundances supply more energy via nuclear burning, inflating the star and increasing its luminosity during early phases. This expansion is more visible at higher accretion rates, where the larger influx of deuterium provides more energy to oppose gravitational contraction.

The birthline: I reproduced the birthline computed by Palla and Stahler (1993), with deviations at the low-mass end where my models are more luminous. This may reflect the choice of seed mass: although nominally similar to that used in the original study, a smaller seed mass might be needed in Cesam2k20 to fully capture the impact of accretion. Additional differences may stem from updated physical ingredients such as the equation of state, opacity tables, and nuclear reaction rates.

Together, these results highlight the importance of incorporating realistic accretion physics when modeling early stellar evolution. While the current implementation omits several physical processes, my work with Cesam2k20 establishes a solid foundation for future studies of PMS evolution.

Several limitations in the current implementation of accretion in Cesam2k20 should be addressed in future work:

seed mass: The use of a relatively large seed mass ($0.1 M_\odot$) is imposed by the available equation of state and opacity tables. Lower seed masses, as used in prior studies

(e.g., Kunitomo et al. (2017)), may produce more pronounced accretion effects and merit exploration.

hot/cold accretion: The current model assumes the extreme case of cold accretion, where all thermal energy is radiated away before the material is accreted. In reality, accretion likely lies somewhere between the extreme cases of hot and cold accretion. Accounting for this heat injection (e.g., Amard and Matt 2023; Hosokawa et al. 2011; Kunitomo et al. 2017) would offer a more realistic picture.

angular momentum: Rotation is currently neglected. Including angular momentum transport could significantly alter the structure and evolution of young stars, with implications for the spin-down problem (e.g., Takasao et al. 2025) and dynamo action (e.g., Stelzer and Neuhäuser 2001).

accretion rate: A constant accretion rate is used in all models, whereas observed protostars often show highly variable accretion. Episodic accretion can leave lasting imprints on the stellar structure and should be investigated in future work (e.g., Baraffe and Chabrier 2010; Baraffe et al. 2009).

convective-radiative boundary: Some models encountered numerical instabilities near the convective-radiative boundary during rapid structural changes. Improving the treatment of this interface is a key focus of my PhD research and will be addressed in future work.

Finally, I note that a parallel branch of the original CESAM code, *Code d'Évolution Planétaire Adaptatif et Modulaire* (CEPAM; Guillot and Morel 1995), has been developed for modeling planetary formation and evolution. A future unification of Cesam2k20 and CEPAM would provide a powerful framework for studying the coupled evolution of young stars and their planetary systems.

Acknowledgements

This internship is part of the [PROMETHEE](#) project funded by the Agence Nationale de la Recherche ([ANR](#)) for the 2023-2026 period. I would like to thank my supervisors, Dr. Ludovic Petitedemange and Dr. João Marques, for their guidance and support throughout this project. I also benefited greatly from discussions with Dr. Louis Manchon, who provided valuable insights into the development of Cesam2k20. I am also grateful to Dr. Charly Pinçon for fruitful discussions during my visits at the IAS. I would also like to thank my office mates, Arthur and Maxime, and the PhD students Virgin, Alexandre, Maxime, and Nathan for their company during the internship. I would also like to thank the members of the [dynamos](#) team for their friendly support and encouragement. Finally, I am thankful to my colleagues at LIRA and LUX—many of whom kindly offered to accommodate me during a difficult period when I was without an office.

References

- Aikawa, M. et al. (2006). “NACRE Update and Extension Project”. In: *Frontiers in Nuclear Structure, Astrophysics, and Reactions*. Vol. 831. AIP, pp. 26–30. DOI: [10.1063/1.2200894](https://doi.org/10.1063/1.2200894).
- Alencar, S. H. P. et al. (2012). “Accretion Dynamics in the Classical T Tauri Star V2129 Ophiuchi”. In: *Astronomy and Astrophysics* 541, A116. DOI: [10.1051/0004-6361/201118395](https://doi.org/10.1051/0004-6361/201118395).
- Amard, L. and S. P. Matt (2023). “Effects of Accretion on the Structure and Rotation of Forming Stars”. In: *Astronomy and Astrophysics* 678, A7. DOI: [10.1051/0004-6361/202346148](https://doi.org/10.1051/0004-6361/202346148).
- Asplund, M., A. M. Amarsi, and N. Grevesse (2021). “The Chemical Make-up of the Sun: A 2020 Vision”. In: *Astronomy and Astrophysics* 653, A141. DOI: [10.1051/0004-6361/202140445](https://doi.org/10.1051/0004-6361/202140445).
- Asplund, M. et al. (2009). “The Chemical Composition of the Sun”. In: *Annual Review of Astronomy and Astrophysics* 47 (Volume 47, 2009), pp. 481–522. DOI: [10.1146/annurev.astro.46.060407.145222](https://doi.org/10.1146/annurev.astro.46.060407.145222).
- Bally, J. (2016). “Protostellar Outflows”. In: *Annual Review of Astronomy and Astrophysics* 54, pp. 491–528. DOI: [10.1146/annurev-astro-081915-023341](https://doi.org/10.1146/annurev-astro-081915-023341).
- Baraffe, I. and G. Chabrier (2010). “Effect of Episodic Accretion on the Structure and the Lithium Depletion of Low-Mass Stars and Planet-Hosting Stars”. In: *Astronomy and Astrophysics* 521, A44. DOI: [10.1051/0004-6361/201014979](https://doi.org/10.1051/0004-6361/201014979).
- Baraffe, I., G. Chabrier, and J. Gallardo (2009). “Episodic Accretion at Early Stages of Evolution of Low-Mass Stars and Brown Dwarfs: A Solution for the Observed Luminosity Spread in H-R Diagrams?” In: *The Astrophysical Journal* 702, pp. L27–L31. DOI: [10.1088/0004-637X/702/1/L27](https://doi.org/10.1088/0004-637X/702/1/L27).
- Baraffe, I., E. Vorobyov, and G. Chabrier (2012). “Observed Luminosity Spread in Young Clusters and FU Ori Stars: A Unified Picture”. In: *The Astrophysical Journal* 756, p. 118. DOI: [10.1088/0004-637X/756/2/118](https://doi.org/10.1088/0004-637X/756/2/118).
- Bouvier, J. (2014). “The Magnetospheric Accretion/Ejection Process in Young Stellar Objects: Open Issues and Perspectives”. In: *European Physical Journal Web of Conferences*. Vol. 64. eprint: arXiv:1310.4439, p. 09001. DOI: [10.1051/epjconf/20136409001](https://doi.org/10.1051/epjconf/20136409001).
- Bouvier, J. et al. (2007). *Magnetospheric Accretion in Classical T Tauri Stars*. DOI: [10.48550/arXiv.astro-ph/0603498](https://doi.org/10.48550/arXiv.astro-ph/0603498). URL: <https://ui.adsabs.harvard.edu/abs/2007prpl.conf..479B>. Pre-published.
- Broggini, C. et al. (2018). “LUNA: Status and Prospects”. In: *Progress in Particle and Nuclear Physics* 98, pp. 55–84. DOI: [10.1016/j.pnpnp.2017.09.002](https://doi.org/10.1016/j.pnpnp.2017.09.002).
- Cox, J. P. and R. T. Giuli (1968). *Principles of Stellar Structure*.
- Eggleton, P. P. (1971). “The Evolution of Low Mass Stars”. In: *Monthly Notices of the Royal Astronomical Society* 151, p. 351. DOI: [10.1093/mnras/151.3.351](https://doi.org/10.1093/mnras/151.3.351).
- Ferguson, J. W. et al. (2005). “Low-Temperature Opacities”. In: *The Astrophysical Journal* 623, pp. 585–596. DOI: [10.1086/428642](https://doi.org/10.1086/428642).
- Gorti, U. and D. Hollenbach (2009). “Photoevaporation of Circumstellar Disks By Far-Ultraviolet, Extreme-Ultraviolet and X-Ray Radiation from the Central Star”. In: *The Astrophysical Journal* 690, pp. 1539–1552. DOI: [10.1088/0004-637X/690/2/1539](https://doi.org/10.1088/0004-637X/690/2/1539).
- Grevesse, N. and A. J. Sauval (1998). “Standard Solar Composition”. In: *Space Science Reviews* 85, pp. 161–174. DOI: [10.1023/A:1005161325181](https://doi.org/10.1023/A:1005161325181).

- Guillot, T. and P. Morel (1995). “CEPAM: A Code for Modeling the Interiors of Giant Planets.” In: *Astronomy and Astrophysics Supplement Series* 109, pp. 109–123.
- Haft, M., G. Raffelt, and A. Weiss (1994). “Standard and Nonstandard Plasma Neutrino Emission Revisited”. In: *The Astrophysical Journal* 425, p. 222. DOI: [10.1086/173978](https://doi.org/10.1086/173978).
- Hartmann, L., G. Herczeg, and N. Calvet (2016). “Accretion onto Pre-Main-Sequence Stars”. In: *Annual Review of Astronomy and Astrophysics* 54 (Volume 54, 2016), pp. 135–180. DOI: [10.1146/annurev-astro-081915-023347](https://doi.org/10.1146/annurev-astro-081915-023347).
- Hartmann, L. et al. (1998). “Accretion and the Evolution of T Tauri Disks”. In: *The Astrophysical Journal* 495, pp. 385–400. DOI: [10.1086/305277](https://doi.org/10.1086/305277).
- Hayashi, C. (1961). “Stellar Evolution in Early Phases of Gravitational Contraction.” In: *Publications of the Astronomical Society of Japan* 13, pp. 450–452.
- Hébrard, G. et al. (2005). “FUSE Determination of a Low Deuterium Abundance along an Extended Sight Line in the Galactic Disk”. In: *The Astrophysical Journal* 635, pp. 1136–1150. DOI: [10.1086/497574](https://doi.org/10.1086/497574).
- Heney, L. G., R. Lelevier, and R. D. Levée (1955). “The Early Phases of Stellar Evolution”. In: *Publications of the Astronomical Society of the Pacific* 67, p. 154. DOI: [10.1086/126791](https://doi.org/10.1086/126791).
- Heney, L. G. et al. (1959). “A Method for Automatic Computation of Stellar Evolution.” In: *The Astrophysical Journal* 129, p. 628. DOI: [10.1086/146661](https://doi.org/10.1086/146661).
- Herbst, W. et al. (2007). *The Rotation of Young Low-Mass Stars and Brown Dwarfs*. DOI: [10.48550/arXiv.astro-ph/0603673](https://doi.org/10.48550/arXiv.astro-ph/0603673). URL: <https://ui.adsabs.harvard.edu/abs/2007prpl.conf..297H> (visited on 06/10/2025). Pre-published.
- Hosokawa, T., S. S. R. Offner, and M. R. Krumholz (2011). “On the Reliability of Stellar Ages and Age Spreads Inferred from Pre-main-sequence Evolutionary Models”. In: *The Astrophysical Journal* 738, p. 140. DOI: [10.1088/0004-637X/738/2/140](https://doi.org/10.1088/0004-637X/738/2/140).
- Hubeny, I. and D. Mihalas (2015). *Theory of Stellar Atmospheres. An Introduction to Astrophysical Non-equilibrium Quantitative Spectroscopic Analysis*.
- Iben Jr., I. (1965). “Stellar Evolution. I. The Approach to the Main Sequence.” In: *The Astrophysical Journal* 141, p. 993. DOI: [10.1086/148193](https://doi.org/10.1086/148193).
- Iglesias, C. A. and F. J. Rogers (1996). “Updated Opal Opacities”. In: *The Astrophysical Journal* 464, p. 943. DOI: [10.1086/177381](https://doi.org/10.1086/177381).
- Ireland, L. G. et al. (2020). “Magnetic Braking of Accreting T Tauri Stars: Effects of Mass Accretion Rate, Rotation, and Dipolar Field Strength”. In: *The Astrophysical Journal* 906.1, p. 4. DOI: [10.3847/1538-4357/abc828](https://doi.org/10.3847/1538-4357/abc828).
- Kastner, J. H. et al. (2002). “Evidence for Accretion: High-Resolution X-Ray Spectroscopy of the Classical T Tauri Star TW Hydrae”. In: *The Astrophysical Journal* 567, pp. 434–440. DOI: [10.1086/338419](https://doi.org/10.1086/338419).
- Kippenhahn, R., A. Weigert, and A. Weiss (2013). *Stellar Structure and Evolution*. DOI: [10.1007/978-3-642-30304-3](https://doi.org/10.1007/978-3-642-30304-3).
- Koenigl, A. (1991). “Disk Accretion onto Magnetic T Tauri Stars”. In: *The Astrophysical Journal* 370, p. L39. DOI: [10.1086/185972](https://doi.org/10.1086/185972).
- Kunitomo, M. and T. Guillot (2021). “Imprint of Planet Formation in the Deep Interior of the Sun”. In: *Astronomy & Astrophysics* 655, A51. DOI: [10.1051/0004-6361/202141256](https://doi.org/10.1051/0004-6361/202141256).
- Kunitomo, M. et al. (2017). “Revisiting the Pre-Main-Sequence Evolution of Stars - I. Importance of Accretion Efficiency and Deuterium Abundance”. In: *Astronomy & Astrophysics* 599, A49. DOI: [10.1051/0004-6361/201628260](https://doi.org/10.1051/0004-6361/201628260).

- Lanzafame, A. C. et al. (2023). “Gaia Data Release 3. Stellar Chromospheric Activity and Mass Accretion from Ca II IRT Observed by the Radial Velocity Spectrometer”. In: *Astronomy and Astrophysics* 674, A30. DOI: [10.1051/0004-6361/202244156](https://doi.org/10.1051/0004-6361/202244156).
- Larson, R. B. (1969). “Numerical Calculations of the Dynamics of Collapsing Proto-Star”. In: *Monthly Notices of the Royal Astronomical Society* 145, p. 271. DOI: [10.1093/mnras/145.3.271](https://doi.org/10.1093/mnras/145.3.271).
- Lii, P. S. et al. (2014). “Propeller-Driven Outflows from an MRI Disc”. In: *Monthly Notices of the Royal Astronomical Society* 441.1, pp. 86–100. DOI: [10.1093/mnras/stu495](https://doi.org/10.1093/mnras/stu495).
- Linsky, J. L. et al. (2006). “What Is the Total Deuterium Abundance in the Local Galactic Disk?” In: *The Astrophysical Journal* 647, pp. 1106–1124. DOI: [10.1086/505556](https://doi.org/10.1086/505556).
- Maeder, A. (2009). *Physics, Formation and Evolution of Rotating Stars*. DOI: [10.1007/978-3-540-76949-1](https://doi.org/10.1007/978-3-540-76949-1).
- Manara, C. F. et al. (2017). “X-Shooter Study of Accretion in Chamaeleon I. II. A Steeper Increase of Accretion with Stellar Mass for Very Low-Mass Stars?” In: *Astronomy and Astrophysics* 604, A127. DOI: [10.1051/0004-6361/201630147](https://doi.org/10.1051/0004-6361/201630147).
- Manchon, L. (2021). “On the Transport of Angular Momentum in Stellar Radiative Zones in 2D”. PhD thesis. Université Paris-Saclay.
- Marques, J. P. et al. (2013). “Seismic Diagnostics for Transport of Angular Momentum in Stars. I. Rotational Splittings from the Pre-Main Sequence to the Red-Giant Branch”. In: *Astronomy and Astrophysics* 549, A74. DOI: [10.1051/0004-6361/201220211](https://doi.org/10.1051/0004-6361/201220211).
- Morel, P. (1997). “CESAM: A Code for Stellar Evolution Calculations”. In: *Astronomy and Astrophysics Supplement Series* 124, pp. 597–614. DOI: [10.1051/aas:1997209](https://doi.org/10.1051/aas:1997209).
- Morel, P. and Y. Lebreton (2008). “CESAM: A Free Code for Stellar Evolution Calculations”. In: *Astrophysics and Space Science* 316, pp. 61–73. DOI: [10.1007/s10509-007-9663-9](https://doi.org/10.1007/s10509-007-9663-9).
- Muzerolle, J., N. Calvet, and L. Hartmann (2001). “Emission-Line Diagnostics of T Tauri Magnetospheric Accretion. II. Improved Model Tests and Insights into Accretion Physics”. In: *The Astrophysical Journal* 550, pp. 944–961. DOI: [10.1086/319779](https://doi.org/10.1086/319779).
- Muzerolle, J. et al. (2003). “Accretion in Young Stellar/Substellar Objects”. In: *The Astrophysical Journal* 592, pp. 266–281. DOI: [10.1086/375704](https://doi.org/10.1086/375704).
- Palla, F. and S. W. Stahler (1993). “The Pre-Main-Sequence Evolution of Intermediate-Mass Stars”. In: *The Astrophysical Journal* 418, p. 414. DOI: [10.1086/173402](https://doi.org/10.1086/173402).
- Paxton, B. et al. (2015). “Modules for Experiments in Stellar Astrophysics (MESA): Binaries, Pulsations, and Explosions”. In: *The Astrophysical Journal Supplement Series* 220, p. 15. DOI: [10.1088/0067-0049/220/1/15](https://doi.org/10.1088/0067-0049/220/1/15).
- Prantzos, N. (2007). “Origin and Evolution of the Light Nuclides”. In: *Space Science Reviews* 130, pp. 27–42. DOI: [10.1007/s11214-007-9183-5](https://doi.org/10.1007/s11214-007-9183-5).
- Press, W. H. et al. (1992). *Numerical Recipes in FORTRAN. The Art of Scientific Computing*.
- Prialnik, D. and M. Livio (1985). “The Outcome of Accretion on to a Fully Convective Star Expansion or Contraction?” In: *Monthly Notices of the Royal Astronomical Society* 216, pp. 37–52. DOI: [10.1093/mnras/216.1.37](https://doi.org/10.1093/mnras/216.1.37).
- Rogers, F. J. and A. Nayfonov (2002). “Updated and Expanded OPAL Equation-of-State Tables: Implications for Helioseismology”. In: *The Astrophysical Journal* 576, pp. 1064–1074. DOI: [10.1086/341894](https://doi.org/10.1086/341894).
- Rogers, F. J. and C. A. Iglesias (1992). “Rosseland Mean Opacities for Variable Compositions”. In: *The Astrophysical Journal* 401, p. 361. DOI: [10.1086/172066](https://doi.org/10.1086/172066).

- Romanova, M. M. et al. (2004). “The Propeller Regime of Disk Accretion to a Rapidly Rotating Magnetized Star”. In: *The Astrophysical Journal* 616.2, p. L151. DOI: [10.1086/426586](https://doi.org/10.1086/426586).
- Rugel, M., D. Fedele, and G. Herczeg (2018). “X-Shooter Observations of Low-Mass Stars in the η Chamaeleontis Association”. In: *Astronomy and Astrophysics* 609, A70. DOI: [10.1051/0004-6361/201630111](https://doi.org/10.1051/0004-6361/201630111).
- Serenelli, A. M. et al. (2009). “NEW SOLAR COMPOSITION: THE PROBLEM WITH SOLAR MODELS REVISITED”. In: *The Astrophysical Journal* 705.2, p. L123. DOI: [10.1088/0004-637X/705/2/L123](https://doi.org/10.1088/0004-637X/705/2/L123).
- Stahler, S. W. (1983). “The Birthline for Low-Mass Stars.” In: *The Astrophysical Journal* 274, pp. 822–829. DOI: [10.1086/161495](https://doi.org/10.1086/161495).
- Stahler, S. W., F. H. Shu, and R. E. Taam (1980). “The Evolution of Protostars. II - The Hydrostatic Core”. In: *The Astrophysical Journal* 242, pp. 226–241. DOI: [10.1086/158459](https://doi.org/10.1086/158459).
- Stahler, S. W. and F. Palla (2004). *The Formation of Stars*.
- Stelzer, B. and R. Neuhauser (2001). “X-Ray Emission from Young Stars in Taurus-Auriga-Perseus: Luminosity Functions and the Rotation - Activity - Age - Relation”. In: *Astronomy and Astrophysics* 377, pp. 538–556. DOI: [10.1051/0004-6361:20011093](https://doi.org/10.1051/0004-6361:20011093).
- Sugimoto, D. and K. Nomoto (1975). “Thermal Instability of Helium-Burning Shell in Stars Evolving toward Carbon-Detonation Supernovae.” In: *Publications of the Astronomical Society of Japan* 27, pp. 197–213.
- Takasao, S. et al. (2025). “Spin-down of Solar-mass Protostars in Magnetospheric Accretion Paradigm”. In: *The Astrophysical Journal* 980.1, p. 111. DOI: [10.3847/1538-4357/ada364](https://doi.org/10.3847/1538-4357/ada364).
- Vaytet, N. et al. (2013). “Simulations of Protostellar Collapse Using Multigroup Radiation Hydrodynamics. II. The Second Collapse”. In: *Astronomy and Astrophysics* 557, A90. DOI: [10.1051/0004-6361/201321423](https://doi.org/10.1051/0004-6361/201321423).
- Weigert, A. (1966). “Sternentwicklung VI: Entwicklung Mit Neutrinoverlust Und Thermische Pulse Der Helium-Schalenquelle Bei Einem Stern von 5 Sonnenmassen”. In: *Zeitschrift für Astrophysik* 64, p. 395.

The terms in the jacobian relevant to the energy equation

First, I recall the full form of the structure equations in Cesam2k20, including the rotational terms that were omitted in Eq. (26a) in the main text, since rotation is not considered in this work. However, the partial derivatives used in the Newton-Raphson iterations are computed with the rotational terms included, in order to facilitate future extensions of the accretion models that incorporate rotation. The full system of structure equations is given by:

$$0 = \frac{\partial \xi}{\partial q} - \left[-\frac{3G}{8\pi} \left(\frac{M_\odot}{R_\odot} \right)^2 \left(\frac{\mu}{\zeta} \right)^2 + \frac{M_\odot}{4\pi R_\odot} \left(\frac{\mu}{\zeta} \right)^{1/2} \Omega^2 \right] e^{-\xi} \frac{\psi}{\theta}, \quad (\text{A.1a})$$

$$0 = \frac{\partial \eta}{\partial q} - \left[-\frac{3G}{8\pi} \left(\frac{M_\odot}{R_\odot} \right)^2 \left(\frac{\mu}{\zeta} \right)^2 + \frac{M_\odot}{4\pi R_\odot} \left(\frac{\mu}{\zeta} \right)^{1/2} \Omega^2 \right] e^{-\xi} \frac{\psi}{\theta} \nabla, \quad (\text{A.1b})$$

$$0 = \frac{\partial \zeta}{\partial q} - \frac{3}{4\pi} \frac{M_\odot}{R_\odot^3} \frac{1}{\rho} \left(\frac{\mu}{\zeta} \right)^{1/2} \frac{\psi}{\theta}, \quad (\text{A.1c})$$

$$0 = \frac{\partial \lambda}{\partial q} - \frac{M_\odot}{L_\odot} \left(\frac{\mu}{\lambda} \right)^{1/2} (\epsilon - \epsilon_\nu + \epsilon_g) \frac{\psi}{\theta}, \quad (\text{A.1d})$$

$$0 = \frac{\partial \mu}{\partial q} - \frac{\psi}{\theta}, \quad (\text{A.1e})$$

$$0 = \frac{\partial \psi}{\partial q}, \quad (\text{A.1f})$$

$$0 = \frac{\partial X_i}{\partial t} + \frac{2}{3M_\odot \mu^{1/2}} \frac{\partial F_i}{\partial \mu} - \Psi_i(\xi, \eta, \mathbf{X}), 1 \leq i \leq n_{\text{elem}}. \quad (\text{A.1g})$$

For simplicity, I will adopt the following notations:

$$\xi' \equiv \frac{\partial \xi}{\partial q}, \quad \eta' \equiv \frac{\partial \eta}{\partial q}, \quad \zeta' \equiv \frac{\partial \zeta}{\partial q}, \quad \lambda' \equiv \frac{\partial \lambda}{\partial q}, \quad \mu' \equiv \frac{\partial \mu}{\partial q}. \quad (\text{A.2})$$

From the equation of state, we have:

- $c_p = c_p(\xi, \eta, \zeta, \lambda, \mu)$
- $\delta = \delta(\xi, \eta, \zeta, \lambda, \mu)$
- $\rho = \rho(\xi, \eta, \zeta, \lambda, \mu)$

term $\partial T / \partial \mu|_t$

$$\left. \frac{\partial T}{\partial \mu} \right|_t = e^\eta \left[-\frac{3G}{8\pi} \left(\frac{M_\odot}{R_\odot} \right)^2 \left(\frac{\mu}{\zeta} \right)^2 + \frac{M_\odot}{4\pi R_\odot} \left(\frac{\mu}{\zeta} \right)^{1/2} \Omega^2 \right] e^{-\xi} \nabla \Rightarrow \left. \frac{\partial T}{\partial \mu} \right|_t(\xi, \eta, \zeta, \lambda, \mu) \quad (\text{A.3})$$

derivatives:

$$\left. \frac{\partial}{\partial \xi} \frac{\partial T}{\partial \mu} \right|_t = e^\eta \left[-\frac{3G}{8\pi} \left(\frac{M_\odot}{R_\odot} \right)^2 \left(\frac{\mu}{\zeta} \right)^2 + \frac{M_\odot}{4\pi R_\odot} \left(\frac{\mu}{\zeta} \right)^{1/2} \Omega^2 \right] \left(-e^{-\xi} \nabla + e^{-\xi} \frac{\partial \nabla}{\partial \xi} \right) \quad (\text{A.4})$$

$$\left. \frac{\partial}{\partial \eta} \frac{\partial T}{\partial \mu} \right|_t = e^\eta \left[-\frac{3G}{8\pi} \left(\frac{M_\odot}{R_\odot} \right)^2 \left(\frac{\mu}{\zeta} \right)^2 + \frac{M_\odot}{4\pi R_\odot} \left(\frac{\mu}{\zeta} \right)^{1/2} \Omega^2 \right] e^{-\xi} \left(\frac{\partial \nabla}{\partial \eta} + \nabla \right) \quad (\text{A.5})$$

$$\begin{aligned} \left. \frac{\partial}{\partial \zeta} \frac{\partial T}{\partial \mu} \right|_t &= e^\eta \left[-\frac{3G}{8\pi} \left(\frac{M_\odot}{R_\odot} \right)^2 \left(-2 \frac{\mu^2}{\zeta^3} \right) + \frac{M_\odot}{4\pi R_\odot} \left(-\frac{1}{2} \frac{\mu^{1/2}}{\zeta^{3/2}} \right) \Omega^2 \right] e^{-\xi} \nabla \\ &+ e^\eta \left[-\frac{3G}{8\pi} \left(\frac{M_\odot}{R_\odot} \right)^2 \left(\frac{\mu}{\zeta} \right)^2 + \frac{M_\odot}{4\pi R_\odot} \left(\frac{\mu}{\zeta} \right)^{1/2} \Omega^2 \right] e^{-\xi} \frac{\partial \nabla}{\partial \zeta} \end{aligned} \quad (\text{A.6})$$

$$\left. \frac{\partial}{\partial \lambda} \frac{\partial T}{\partial \mu} \right|_t = e^\eta \left[-\frac{3G}{8\pi} \left(\frac{M_\odot}{R_\odot} \right)^2 \left(\frac{\mu}{\zeta} \right)^2 + \frac{M_\odot}{4\pi R_\odot} \left(\frac{\mu}{\zeta} \right)^{1/2} \Omega^2 \right] e^{-\xi} \frac{\partial \nabla}{\partial \lambda} \quad (\text{A.7})$$

$$\begin{aligned} \left. \frac{\partial}{\partial \mu} \frac{\partial T}{\partial \mu} \right|_t &= e^\eta \left[-\frac{3G}{8\pi} \left(\frac{M_\odot}{R_\odot} \right)^2 \left(2 \frac{\mu}{\zeta^2} \right) + \frac{M_\odot}{4\pi R_\odot} \left(\frac{1}{2} \frac{\mu^{-1/2}}{\zeta^{3/2}} \right) \Omega^2 \right] e^{-\xi} \nabla \\ &+ e^\eta \left[-\frac{3G}{8\pi} \left(\frac{M_\odot}{R_\odot} \right)^2 \left(\frac{\mu}{\zeta} \right)^2 + \frac{M_\odot}{4\pi R_\odot} \left(\frac{\mu}{\zeta} \right)^{1/2} \Omega^2 \right] e^{-\xi} \frac{\partial \nabla}{\partial \mu} \end{aligned} \quad (\text{A.8})$$

term $\partial p / \partial \mu|_t$

$$\left. \frac{\partial p}{\partial \mu} \right|_t = \left[-\frac{3G}{8\pi} \left(\frac{M_\odot}{R_\odot} \right)^2 \left(\frac{\mu}{\zeta} \right)^2 + \frac{M_\odot}{4\pi R_\odot} \left(\frac{\mu}{\zeta} \right)^{1/2} \Omega^2 \right] \Rightarrow \left. \frac{\partial p}{\partial \mu} \right|_t (\zeta, \mu) \quad (\text{A.9})$$

derivatives:

$$\left. \frac{\partial}{\partial \zeta} \frac{\partial p}{\partial \mu} \right|_t = \left[-\frac{3G}{8\pi} \left(\frac{M_\odot}{R_\odot} \right)^2 \left(-2 \frac{\mu^2}{\zeta^3} \right) + \frac{M_\odot}{4\pi R_\odot} \left(-\frac{1}{2} \frac{\mu^{1/2}}{\zeta^{3/2}} \right) \Omega^2 \right] \quad (\text{A.10})$$

$$\left. \frac{\partial}{\partial \mu} \frac{\partial p}{\partial \mu} \right|_t = \left[-\frac{3G}{8\pi} \left(\frac{M_\odot}{R_\odot} \right)^2 \left(2 \frac{\mu}{\zeta^2} \right) + \frac{M_\odot}{4\pi R_\odot} \left(\frac{1}{2} \frac{\mu^{-1/2}}{\zeta^{1/2}} \right) \Omega^2 \right] \quad (\text{A.11})$$

the derivatives of $T \partial s / \partial t$

- with respect to ξ

$$\begin{aligned} \frac{\partial}{\partial \xi} \left(T \frac{\partial s}{\partial t} \right) &= \left\{ \frac{\partial c_p}{\partial \xi} (T_{\mu_x} - T_{\mu_x}^t) + c_p \left(\frac{\partial T_{\mu_x}}{\partial \xi} - \frac{\partial T_{\mu_x}^t}{\partial \xi} \right) \right. \\ &\quad \left. - \frac{\delta}{\rho} \left[\left(\frac{1}{\delta} \frac{\partial \delta}{\partial \xi} - \frac{1}{\rho^2} \frac{\partial \rho}{\partial \xi} \right) (p_{\mu_x} - p_{\mu_x}^t) + \left(\frac{\partial p_{\mu_x}}{\partial \xi} - \frac{\partial p_{\mu_x}^t}{\partial \xi} \right) \right] \right\} \frac{1}{dt} \\ &- \frac{2}{3} \dot{M} \frac{M_\odot^{2/3}}{M_2^{5/3}} \mu \left. \frac{\partial \mu}{\partial \mu_x} \right|_t \left\{ \frac{\partial c_p}{\partial \xi} \frac{\partial T}{\partial \mu} \right|_t + c_p \frac{\partial}{\partial \xi} \frac{\partial T}{\partial \mu} \Big|_t - \left(\frac{1}{\rho} \frac{\partial \delta}{\partial \xi} \frac{\partial p}{\partial \mu} \Big|_t - \frac{\delta}{\rho^2} \frac{\partial \rho}{\partial \xi} \frac{\partial p}{\partial \mu} \Big|_t + \frac{\delta}{\rho} \frac{\partial}{\partial \xi} \frac{\partial p}{\partial \mu} \Big|_t \right) \Big\} \\ &= \left\{ \frac{\partial c_p}{\partial \xi} (T_{\mu_x} - T_{\mu_x}^t) - \frac{\delta}{\rho} \left[\left(\frac{1}{\delta} \frac{\partial \delta}{\partial \xi} - \frac{1}{\rho^2} \frac{\partial \rho}{\partial \xi} \right) (p_{\mu_x} - p_{\mu_x}^t) + \frac{\partial p_{\mu_x}}{\partial \xi} \right] \right\} \frac{1}{dt} \\ &- \frac{2}{3} \dot{M} \frac{M_\odot^{2/3}}{M_2^{5/3}} \mu \left. \frac{\partial \mu}{\partial \mu_x} \right|_t \left\{ \frac{\partial c_p}{\partial \xi} \frac{\partial T}{\partial \mu} \Big|_t + c_p \frac{\partial}{\partial \xi} \frac{\partial T}{\partial \mu} \Big|_t - \frac{\delta}{\rho} \left(\frac{1}{\delta} \frac{\partial \delta}{\partial \xi} - \frac{1}{\rho} \frac{\partial \rho}{\partial \xi} \right) \frac{\partial p}{\partial \mu} \Big|_t \right\} \end{aligned} \quad (\text{A.12})$$

- with respect to η

$$\begin{aligned}
\frac{\partial}{\partial \eta} \left(T \frac{\partial s}{\partial t} \right) &= \left\{ \frac{\partial c_p}{\partial \eta} (T_{\mu_x} - T_{\mu_x}^t) + c_p \left(\frac{\partial T_{\mu_x}}{\partial \eta} - \frac{\partial T_{\mu_x}^t}{\partial \eta} \right) \right. \\
&\quad \left. - \frac{\delta}{\rho} \left[\left(\frac{1}{\delta} \frac{\partial \delta}{\partial \eta} - \frac{1}{\rho^2} \frac{\partial \rho}{\partial \eta} \right) (p_{\mu_x} - p_{\mu_x}^t) + \left(\frac{\partial p_{\mu_x}}{\partial \eta} - \frac{\partial p_{\mu_x}^t}{\partial \eta} \right) \right] \right\} \frac{1}{dt} \\
&- \frac{2}{3} \dot{M} \frac{M_{\odot}^{2/3}}{M_2^{5/3}} \mu \frac{\partial \mu}{\partial \mu_x} \Big|_t \left\{ \frac{\partial c_p}{\partial \eta} \frac{\partial T}{\partial \mu} \Big|_t + c_p \frac{\partial}{\partial \eta} \frac{\partial T}{\partial \mu} \Big|_t - \left(\frac{1}{\rho} \frac{\partial \delta}{\partial \eta} \frac{\partial p}{\partial \mu} \Big|_t - \frac{\delta}{\rho^2} \frac{\partial \rho}{\partial \eta} \frac{\partial p}{\partial \mu} \Big|_t + \frac{\delta}{\rho} \frac{\partial}{\partial \eta} \frac{\partial p}{\partial \mu} \Big|_t \right) \right\} \\
&= \left\{ \frac{\partial c_p}{\partial \eta} (T_{\mu_x} - T_{\mu_x}^t) + c_p \frac{\partial T_{\mu_x}}{\partial \eta} - \frac{\delta}{\rho} \left[\left(\frac{1}{\delta} \frac{\partial \delta}{\partial \eta} - \frac{1}{\rho^2} \frac{\partial \rho}{\partial \eta} \right) (p_{\mu_x} - p_{\mu_x}^t) \right] \right\} \frac{1}{dt} \\
&- \frac{2}{3} \dot{M} \frac{M_{\odot}^{2/3}}{M_2^{5/3}} \mu \frac{\partial \mu}{\partial \mu_x} \Big|_t \left\{ \frac{\partial c_p}{\partial \eta} \frac{\partial T}{\partial \mu} \Big|_t + c_p \frac{\partial}{\partial \eta} \frac{\partial T}{\partial \mu} \Big|_t - \frac{\delta}{\rho} \left(\frac{1}{\delta} \frac{\partial \delta}{\partial \eta} - \frac{1}{\rho} \frac{\partial \rho}{\partial \eta} \right) \frac{\partial p}{\partial \mu} \Big|_t \right\} \quad (A.13)
\end{aligned}$$

- with respect to ζ

$$\begin{aligned}
\frac{\partial}{\partial \zeta} \left(T \frac{\partial s}{\partial t} \right) &= \left\{ \frac{\partial c_p}{\partial \zeta} (T_{\mu_x} - T_{\mu_x}^t) + c_p \left(\frac{\partial T_{\mu_x}}{\partial \zeta} - \frac{\partial T_{\mu_x}^t}{\partial \zeta} \right) \right. \\
&\quad \left. - \frac{\delta}{\rho} \left[\left(\frac{1}{\delta} \frac{\partial \delta}{\partial \zeta} - \frac{1}{\rho^2} \frac{\partial \rho}{\partial \zeta} \right) (p_{\mu_x} - p_{\mu_x}^t) + \left(\frac{\partial p_{\mu_x}}{\partial \zeta} - \frac{\partial p_{\mu_x}^t}{\partial \zeta} \right) \right] \right\} \frac{1}{dt} \\
&- \frac{2}{3} \dot{M} \frac{M_{\odot}^{2/3}}{M_2^{5/3}} \mu \frac{\partial \mu}{\partial \mu_x} \Big|_t \left\{ \frac{\partial c_p}{\partial \zeta} \frac{\partial T}{\partial \mu} \Big|_t + c_p \frac{\partial}{\partial \zeta} \frac{\partial T}{\partial \mu} \Big|_t - \left(\frac{1}{\rho} \frac{\partial \delta}{\partial \zeta} \frac{\partial p}{\partial \mu} \Big|_t - \frac{\delta}{\rho^2} \frac{\partial \rho}{\partial \zeta} \frac{\partial p}{\partial \mu} \Big|_t + \frac{\delta}{\rho} \frac{\partial}{\partial \zeta} \frac{\partial p}{\partial \mu} \Big|_t \right) \right\} \\
&= -\frac{2}{3} \dot{M} \frac{M_{\odot}^{2/3}}{M_2^{5/3}} \mu \frac{\partial \mu}{\partial \mu_x} \Big|_t \left\{ c_p \frac{\partial}{\partial \zeta} \frac{\partial T}{\partial \mu} \Big|_t - \frac{\delta}{\rho} \frac{\partial}{\partial \zeta} \frac{\partial p}{\partial \mu} \Big|_t \right\} \quad (A.14)
\end{aligned}$$

- with respect to λ

$$\begin{aligned}
\frac{\partial}{\partial \lambda} \left(T \frac{\partial s}{\partial t} \right) &= \left\{ \frac{\partial c_p}{\partial \lambda} (T_{\mu_x} - T_{\mu_x}^t) + c_p \left(\frac{\partial T_{\mu_x}}{\partial \lambda} - \frac{\partial T_{\mu_x}^t}{\partial \lambda} \right) \right. \\
&\quad \left. - \frac{\delta}{\rho} \left[\left(\frac{1}{\delta} \frac{\partial \delta}{\partial \lambda} - \frac{1}{\rho^2} \frac{\partial \rho}{\partial \lambda} \right) (p_{\mu_x} - p_{\mu_x}^t) + \left(\frac{\partial p_{\mu_x}}{\partial \lambda} - \frac{\partial p_{\mu_x}^t}{\partial \lambda} \right) \right] \right\} \frac{1}{dt} \\
&- \frac{2}{3} \dot{M} \frac{M_{\odot}^{2/3}}{M_2^{5/3}} \mu \frac{\partial \mu}{\partial \mu_x} \Big|_t \left\{ \frac{\partial c_p}{\partial \lambda} \frac{\partial T}{\partial \mu} \Big|_t + c_p \frac{\partial}{\partial \lambda} \frac{\partial T}{\partial \mu} \Big|_t - \left(\frac{1}{\rho} \frac{\partial \delta}{\partial \lambda} \frac{\partial p}{\partial \mu} \Big|_t - \frac{\delta}{\rho^2} \frac{\partial \rho}{\partial \lambda} \frac{\partial p}{\partial \mu} \Big|_t + \frac{\delta}{\rho} \frac{\partial}{\partial \lambda} \frac{\partial p}{\partial \mu} \Big|_t \right) \right\} \\
&= -\frac{2}{3} \dot{M} \frac{M_{\odot}^{2/3}}{M_2^{5/3}} \mu \frac{\partial \mu}{\partial \mu_x} \Big|_t \left\{ c_p \frac{\partial}{\partial \lambda} \frac{\partial T}{\partial \mu} \Big|_t \right\} \quad (A.15)
\end{aligned}$$

- with respect to μ

$$\begin{aligned}
& \frac{\partial}{\partial \mu} \left(T \frac{\partial s}{\partial t} \right) = \left\{ \frac{\partial c_p}{\partial \mu} (T_{\mu_x} - T_{\mu_x}^t) + c_p \left(\frac{\partial T_{\mu_x}}{\partial \mu} - \frac{\partial T_{\mu_x}^t}{\partial \mu} \right) \right. \\
& \quad \left. - \frac{\delta}{\rho} \left[\left(\frac{1}{\delta} \frac{\partial \delta}{\partial \mu} - \frac{1}{\rho^2} \frac{\partial \rho}{\partial \mu} \right) (p_{\mu_x} - p_{\mu_x}^t) + \left(\frac{\partial p_{\mu_x}}{\partial \mu} - \frac{\partial p_{\mu_x}^t}{\partial \mu} \right) \right] \right\} \frac{1}{dt} \\
& - \frac{2}{3} \dot{M} \frac{M_{\odot}^{2/3}}{M_2^{5/3}} \mu \frac{\partial \mu}{\partial \mu_x} \Big|_t \left\{ \frac{\partial c_p}{\partial \mu} \frac{\partial T}{\partial \mu} \Big|_t + c_p \frac{\partial}{\partial \mu} \frac{\partial T}{\partial \mu} \Big|_t - \left(\frac{1}{\rho} \frac{\partial \delta}{\partial \mu} \frac{\partial p}{\partial \mu} \Big|_t - \frac{\delta}{\rho^2} \frac{\partial \rho}{\partial \mu} \frac{\partial p}{\partial \mu} \Big|_t + \frac{\delta}{\rho} \frac{\partial}{\partial \mu} \frac{\partial p}{\partial \mu} \Big|_t \right) \right\} \\
& - \frac{2}{3} \dot{M} \frac{M_{\odot}^{2/3}}{M_2^{5/3}} \frac{\partial \mu}{\partial \mu_x} \Big|_t \left(c_p \frac{\partial T}{\partial \mu} \Big|_t - \frac{\delta}{\rho} \frac{\partial p}{\partial \mu} \Big|_t \right) \\
& = \left\{ \frac{\partial c_p}{\partial \mu} (T_{\mu_x} - T_{\mu_x}^t) - c_p \frac{\partial T_{\mu_x}^t}{\partial \mu} - \frac{\delta}{\rho} \left[\left(\frac{1}{\delta} \frac{\partial \delta}{\partial \mu} - \frac{1}{\rho^2} \frac{\partial \rho}{\partial \mu} \right) (p_{\mu_x} - p_{\mu_x}^t) - \frac{\partial p_{\mu_x}^t}{\partial \mu} \right] \right\} \frac{1}{dt} \\
& - \frac{2}{3} \dot{M} \frac{M_{\odot}^{2/3}}{M_2^{5/3}} \mu \frac{\partial \mu}{\partial \mu_x} \Big|_t \left\{ \frac{\partial c_p}{\partial \mu} \frac{\partial T}{\partial \mu} \Big|_t + c_p \frac{\partial}{\partial \mu} \frac{\partial T}{\partial \mu} \Big|_t - \frac{\delta}{\rho} \left[\left(\frac{1}{\delta} \frac{\partial \delta}{\partial \mu} - \frac{1}{\rho^2} \frac{\partial \rho}{\partial \mu} \right) \frac{\partial p}{\partial \mu} \Big|_t + \frac{\partial}{\partial \mu} \frac{\partial p}{\partial \mu} \Big|_t \right] \right\} \\
& - \frac{2}{3} \dot{M} \frac{M_{\odot}^{2/3}}{M_2^{5/3}} \frac{\partial \mu}{\partial \mu_x} \Big|_t \left(c_p \frac{\partial T}{\partial \mu} \Big|_t - \frac{\delta}{\rho} \frac{\partial p}{\partial \mu} \Big|_t \right) \tag{A.16}
\end{aligned}$$